Extreme Convective Rainfall and Flooding from Winter Season Extratropical Cyclones in the Mid-Atlantic Region of the United States

YIBING SU,[a] JAMES A. SMITH,[a] AND GABRIELE VILLARINI[b]

[a] *Department of Civil and Environmental Engineering, Princeton University, Princeton, New Jersey*
[b] *IIHR–Hydroscience and Engineering, The University of Iowa, Iowa City, Iowa*

ABSTRACT: Extreme rainfall from extratropical cyclones and the distinctive hydrology of the winter season both contribute to flood extremes in the Mid-Atlantic region. In this study, we examine extreme rainfall and flooding from a winter season extratropical cyclone that passed through the eastern United States on 24/25 February 2016. Extreme rainfall rates during the 24/25 February 2016 time period were produced by supercell thunderstorms; we identify supercells through local maxima in azimuthal shear fields computed from Doppler velocity measurements from WSR-88D radars. Rainfall rates approaching 250 mm h^{-1} from a long-lived supercell in New Jersey were measured by a Parsivel disdrometer. A distinctive element of the storm environment for the 24/25 February 2016 storm was elevated values of convective available potential energy (CAPE). We also examine the climatology of atmospheric rivers (ARs)—like the February 2016 storm—based on an identification and tracking algorithm that uses Twentieth Century Reanalysis fields for the 66-yr period from 1950 to 2015. Climatological analyses suggest that AR frequency is increasing over the Mid-Atlantic region. An increase in AR frequency, combined with increasing frequency of elevated CAPE during the winter season over the Mid-Atlantic region, could result in striking changes to the climatology of extreme floods.

KEYWORDS: Atmospheric river; Extratropical cyclones; Extreme events; Flood events; Supercells; CAPE

1. Introduction

Winter season extratropical cyclones have been identified as agents of extreme floods in the Mid-Atlantic and northeastern United States, with the St. Patrick's Day Storm of March 1936 providing a central piece of Miller's "Three Floods" paradigm for eastern U.S. rivers (Miller 1990). Comparable flooding in the Potomac, Susquehanna, and Delaware Rivers resulted from a powerful extratropical cyclone that moved through the region on 18 January 1996. The January 1996 floods were the result of rapid snowmelt punctuated by runoff from intense, short-duration rainfall (Barros and Kuligowski 1998; Grote 2021). In this study, we focus on extreme rainfall and flooding from a winter season extratropical cyclone that passed through the eastern United States on 24/25 February 2016.

Extreme convective rainfall was an important ingredient of flooding for the March 1936, January 1996, and February 2016 events [see Zipser and Liu (2021) for a summary of the links between convective intensity and extreme rainfall]. The exceptional observational data available for the February 2016 event provide the capability to assess key mechanisms resulting in extreme rainfall from winter season extratropical cyclones in the Mid-Atlantic. Analyses cover a range of scales, from synoptic-scale processes that determine the convective environment to cloud-scale processes that drive extreme rainfall rates.

The March 1936, January 1996, and February 2016 storms were linked to major winter-season atmospheric river (AR) episodes for the eastern United States [see Ralph et al. (2020) for a survey of ARs]. The Glossary of Meteorology (American Meteorological Society 2022) defines an AR as "a long, narrow, and transient corridor of strong horizontal water vapor transport that is typically associated with a low-level jet stream ahead of the cold front of an extratropical cyclone" [see Newell et al. (1992) and Zhu and Newell (1998) for early analyses]. Heavy precipitation from ARs in the eastern United States has received less attention than in the western United States (Moore et al. 2012; Mahoney et al. 2016). Our climatological analyses of ARs in the eastern United States are based on an identification and tracking algorithm (Nayak and Villarini 2017; Guan and Waliser 2015; Shields et al. 2018) and Twentieth Century Reanalysis version 3 (20CRV3) fields for the 66-yr period from 1950 to 2015 (Compo et al. 2011). We examine the climatology of ARs in the eastern United States, focusing on the Mid-Atlantic and northeastern U.S. regions affected by the January 1996, February 2016, and March 1936 storms. Climatological analyses focus on the seasonal and the spatial distributions of AR occurrence (Dettinger et al. 2011; Lavers and Villarini 2013; Slinskey et al. 2020), as well as long-term trends in AR properties (Payne et al. 2020).

Rainfall analyses for the February 2016 storm are based on high-resolution polarimetric radar rainfall fields from WSR-88D (Weather Surveillance Radar-1988 Doppler) radars in Sterling, Virginia (VA), and Fort Dix, New Jersey (NJ) [see Kumjian (2013) and Ryzhkov et al. (2022) for summary of polarimetric methods used for rainfall estimation and storm analyses]. Rapid low-elevation scans (Kumjian et al. 2010; Kingfield and French 2022) from the radars are used to estimate rainfall rate fields at 2–3-min time resolution. Rapid scanning strategies are especially important for rainfall analyses of rapidly moving storms (Chaney et al. 2022).

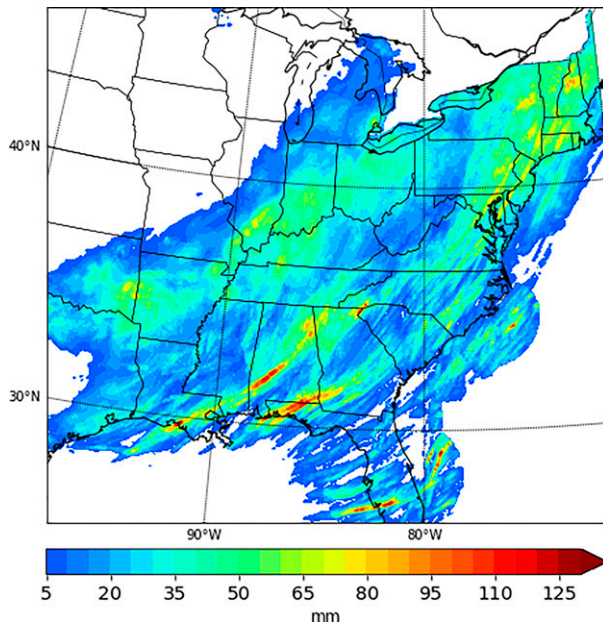*Corresponding author*: Yibing Su, yibings@princeton.edu

FIG. 1. Map showing the 48-h rainfall accumulation (mm) computed from Stage IV radar rainfall fields from 1200 UTC 23 Feb to 1200 UTC 25 Feb 2016.

Extreme rainfall rates during the 24/25 February 2016 time period were produced by supercell thunderstorms, i.e., storms characterized by the presence of a mesocyclone—a deep, persistently rotating updraft (American Meteorological Society 2022; see also Markowski and Richardson 2011). The track and evolution of these storms played a central role in the spatial and temporal distribution of extreme rainfall. Extreme rainfall from the February 2016 storm system was associated with both long-lived supercells (Bunkers et al. 2006; Davenport 2021) and clusters of supercells (Knupp et al. 2014). Physical arguments for amplification of rainfall in supercells are grounded in a source of positive vertical momentum produced by pressure perturbations in the rotating storm (Doswell et al. 1996; Nielsen and Schumacher 2020a). Based on numerical simulations, Nielsen and Schumacher (2018) conclude that low-level rotation can enhance updrafts and produce significantly larger rainfall accumulations than would occur in nonrotating storms.

Changing flood hazards from extratropical cyclones in a warming climate will reflect the mix of hydrometeorological processes driving extreme rainfall and hydrologic processes controlling winter season soil moisture and snowpack. Kunkel et al. (2012) point to increasing trends in daily rainfall extremes from extratropical cyclones. Su and Smith (2021) identify significant increases in extremes of vertically integrated water vapor flux, a key ingredient of extreme rainfall from AR episodes.

Increasing convective intensity in a warming climate (Diffenbaugh et al. 2013; Song et al. 2022) holds potential for increasing extreme rainfall at super-Clausius–Clapeyron rates (Westra et al. 2014; Fowler et al. 2021). The 24/25 February 2016 storm provides an end-member example of extreme convective

rainfall in the northeastern United States during the winter season. The pairing of ARs with elevated values of CAPE provides a recipe for rainfall extremes revolving around the properties of organized convection [see Monteverdi et al. (2003), Oakley et al. (2017), and Huang et al. (2020) for related analyses along the west coast of the United States]. Storm environment plays a central role in dictating convective organization, size of extreme rain areas and storm motion, as reflected in the climatology of extreme winter/spring rainfall in the Southern Plains and southern United States (Mahoney et al. 2016; Schumacher and Rasmussen 2020; Nielsen and Schumacher 2020b).

A primary question that we address in this study is how physical mechanisms linking extratropical cyclones, atmospheric rivers, and convective rainfall combine to produce extreme winter season flooding in the Mid-Atlantic region. In addition, we examine how the climatology of ARs will contribute to the future occurrence of the largest winter-season flood events?

Contents of the paper are organized as follows. In section 2, we introduce the principal datasets and methods employed to examine rainfall extremes. Analyses of storm environment, rainfall and flooding from the 24/25 February 2016 AR episode are presented in section 3. Climatological analyses of ARs in the Mid-Atlantic region are presented in section 4. Discussion of extratropical cyclones and the hydroclimatology of extreme winter season flooding in the Mid-Atlantic is presented in section 5, focusing on record flooding in March 1936 and January 1996. A summary and conclusions are presented in section 6.

2. Data and methods

a. The atmospheric water balance and atmospheric river identification

Precipitable water is the storage term in the *atmospheric water balance equation*; time changes in precipitable water are balanced by additions from surface evaporation, losses from precipitation and water vapor convergence:

$$\frac{\partial W}{\partial t} = E - P - 3600 \nabla \cdot \mathbf{Q}; (\text{mm h}^{-1}), \qquad (1)$$

where P is the precipitation rate (mm h^{-1}), E is the evaporation rate (mm h^{-1}), W is the precipitable water (mm), and $\mathbf{Q} = (Q_x, Q_y)$ is the vertically integrated water vapor flux vector (kg s^{-1} m^{-1}):

$$Q_x = \int_0^{z_t} \rho_v(z) \, u(z) \, dz, \qquad (2)$$

$$Q_y = \int_0^{z_t} \rho_v(z) \, v(z) \, dz, \qquad (3)$$

where $u(z)$ is the east–west component of the wind (m s^{-1}; positive eastward) at elevation z and $v(z)$ is the north–south component of the wind (m s^{-1}; positive to the north) at
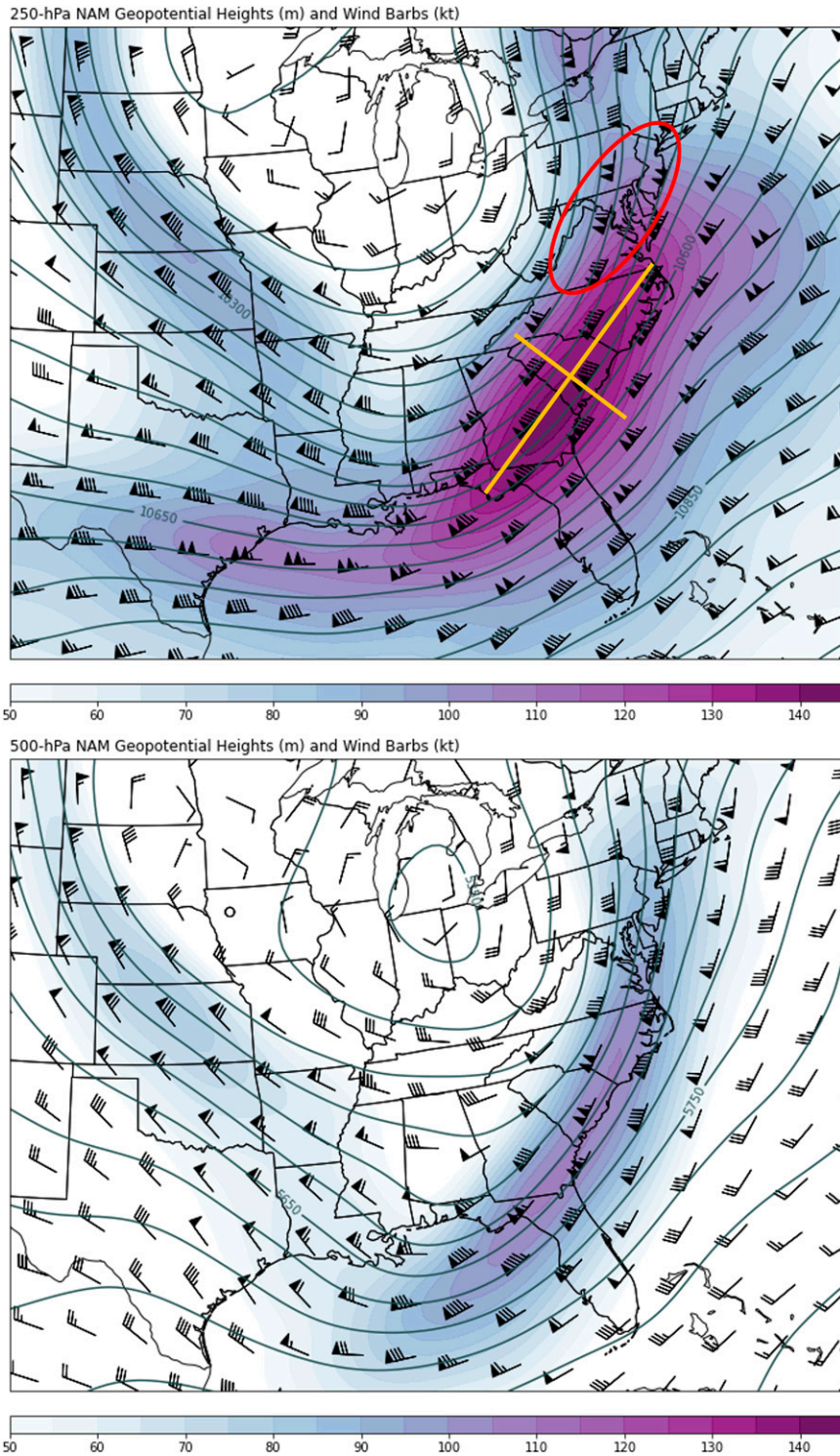
250-hPa NAM Geopotential Heights (m) and Wind Barbs (kt)

500-hPa NAM Geopotential Heights (m) and Wind Barbs (kt)

FIG. 2. (top) 250- and (bottom) 500-hPa geopotential heights (m; as gray contour lines) and wind barbs (kt; 1 kt ≈ 0.51 m s^{-1}) at 0300 UTC 25 Feb 2016 (from NARR). Yellow axes divide the jet streak into four sectors; the red ellipse marks the left exit region, which is associated with lower-level convergence.
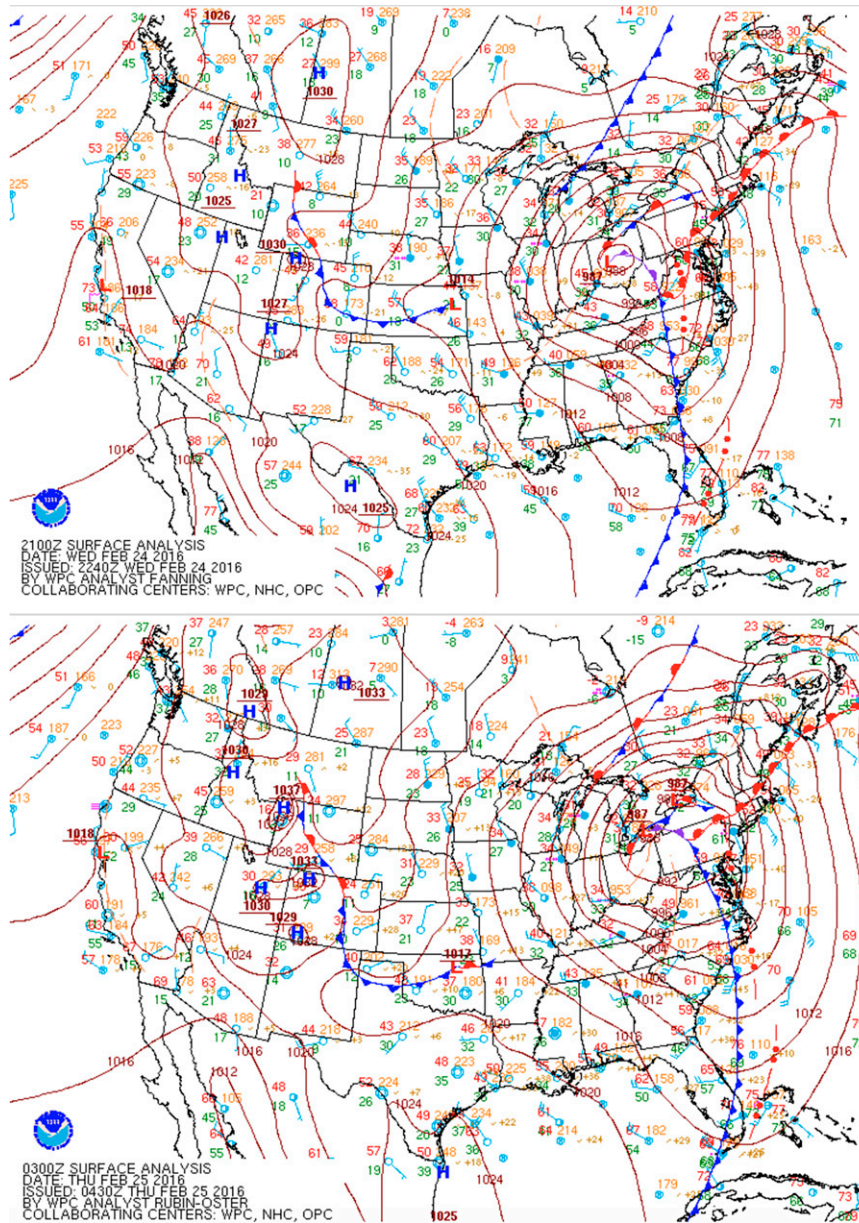
FIG. 3. NWS Storm Prediction Center surface weather maps (National Weather Service) for (top) 1800 UTC 24 Feb and (bottom) 0300 UTC 25 Feb.

elevation z. The magnitude of $\mathbf{Q}$ is the vertically integrated water vapor transport (IVT):

$$\text{IVT} = (Q_x^2 + Q_y^2)^{1/2}. \tag{4}$$

To assess the atmospheric moisture environment during the 2016 event, we compute precipitable water and the vertically integrated water vapor flux using the 3-hourly 32-km resolution specific humidity, wind, surface pressure, and height fields from North American Regional Reanalysis (NARR; Mesinger et al. 2006). NARR provides temporally continuous

fields over the contiguous United States (CONUS) starting in 1979.

Su and Smith (2021) developed a methodology for assessing environmental anomalies in precipitable water and IVT using 10-yr return period fields derived from 40 years of annual maxima computed from NARR (see also Grumm et al. 2005). We employ this approach to examine anomalies of the atmospheric water balance for the February 2016 storm.

To further assess the large-scale atmospheric water vapor transport environment during the event, we employ an AR identification algorithm using the 2016 NARR fields. The
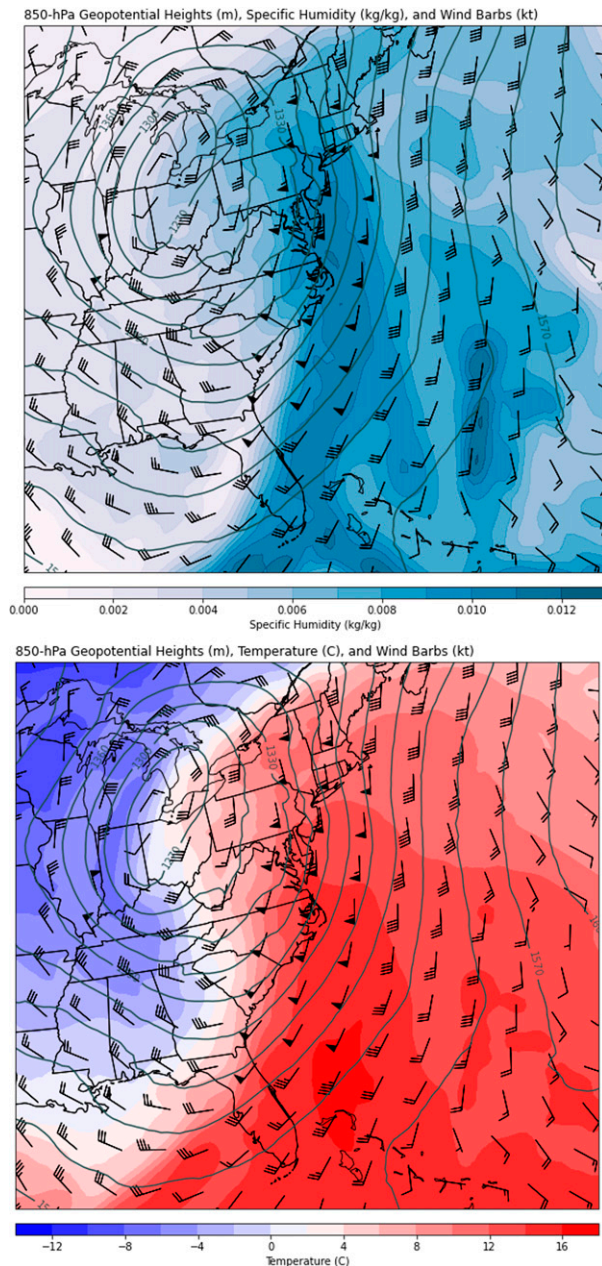
FIG. 4. NARR 850-hPa geopotential heights (m; gray contours), wind barbs (kt), with (top) specific humidity (kg kg^{-1}; color fill) and (bottom) temperature (°C; color fill) at 0000 UTC 25 Feb 2016.

algorithm adopts elements from Nayak and Villarini (2017), with main criteria being a constant IVT threshold of 500 kg s^{-1} m^{-1}, a length threshold of 1000 km and a persistence criterion of 18 h. The algorithm is used to search all central and eastern U.S. ARs from 34° to 45°N, over the longitude band from 100° to 70°W. Each identified AR is tracked south to 20°N and north to 57°N.

We examine the climatology of ARs in the eastern United States, with a focus on ARs that pass through a 1° × 1° box centered on Princeton, NJ (40.357°N, 74.667°W), at any point

in their life cycles. ARs are identified using twentieth century Reanalysis fields from 1950 to 2015 as it offers a longer record period than NARR (Compo et al. 2011; Slivinski et al. 2019). The version 3 reanalysis fields (20CRV3) have 3-hourly and 1° resolution. For assessment of the storm environment during major floods in March 1936 and January 1996, we apply the same AR identification algorithm to 20CRV3 fields.

From the 66-yr catalog of Princeton, NJ, ARs, we assess long-term trends in atmospheric river properties—annual count, length (km), duration (hours), and peak magnitude (IVT in kg s^{-1} m^{-1}). We use the Mann–Kendall test to assess the significance of monotonic trends and the Sen's slope estimator (Helsel and Hirsch 1993) to quantify the magnitudes of trends. The Mann–Kendall test and the Sen's slope estimation are performed in R using the freely available "trend" package (Pohlert 2018).

b. Rainfall measurement

A Parsivel-2 disdrometer located in Princeton, NJ (Smith et al. 2009), recorded raindrop size distributions for the February 2016 storm for 30-s time increments. From the size distribution measurements, we computed rainfall rate, rain drop number density N_t (drops m^{-3}), and volume-weighted median diameter D_0 (mm).

Radar rainfall estimates are constructed from WSR-88D polarimetric radar fields derived from the Fort Dix radar in New Jersey (KDIX) and the Sterling radar in Virginia (KLWX). The principal volume scan polarimetric measurements that we use are horizontal reflectivity Z and differential phase shift ϕ_{DP} (°). The specific differential phase shift K_{DP} (° km^{-1}) is the range derivative of ϕ_{DP}; we compute K_{DP} using the Bringi method implemented in Colorado State University (CSU) Radar Tools (Lang et al. 2007; Wang and Chandrasekar 2009; Reimel and Kumjian 2021).

Volume-scan polarimetric radar fields are converted to Cartesian grids with 0.5-km resolution using the Python ARM Radar Toolkit routines (Py-ART; Helmus and Collis 2016). Rain rate fields are computed from all low-elevation scans. The time resolution of low-elevation scans is approximately 2–3 min. Multiple low-elevation scans within a volume scan were implemented for the WSR-88D system through the SAILS (Supplemental Adaptive Intravolume Low-Level Scan) and MESO-SAILS (Multiple Elevation Scan Option for SAILS) scanning strategies (Kumjian et al. 2010; Kingfield and French 2022). Although principally targeting tornado and severe weather forecasts (see, e.g., Van Den Broeke 2015), the multiple low-elevation scan strategies provide critical insights to rainfall variability, especially for watersheds experiencing extreme, short-duration rainfall (Chaney et al. 2022).

We focus on K_{DP} estimates of extreme rainfall, with horizontal reflectivity Z used for estimating lower rain rates [see Ryzhkov et al. (2022) for a survey of polarimetric methods for rainfall estimation]. We follow previous studies (see, e.g., Chandrasekar et al. 1990) in using a K_{DP} power law equation when reflectivity is large and K_{DP} noise is modest. Specifically, for reflectivity
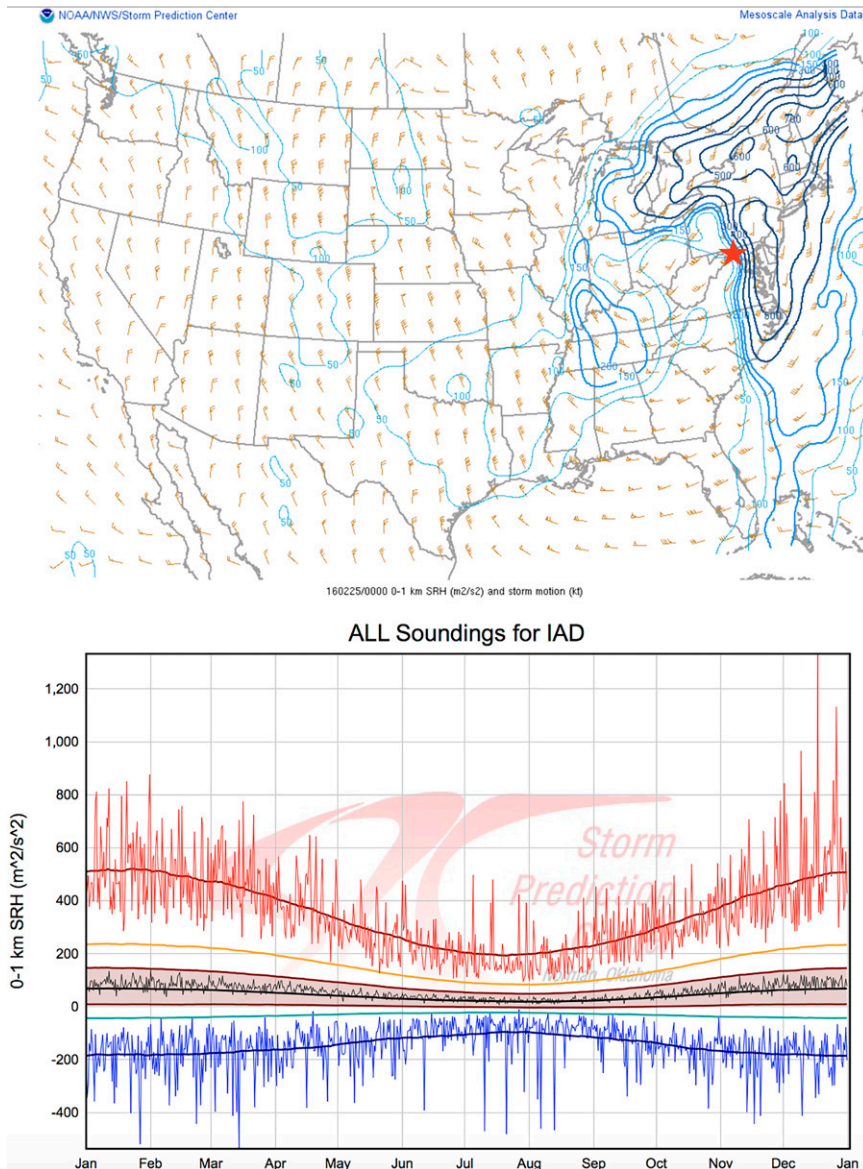
FIG. 5. (top) Storm relative helicity field from the Storm Prediction Center at 0000 UTC 25 Feb (https://www.spc.noaa.gov/exper/archive/events/). (bottom) The climatology of storm relative helicity from Sterling, VA, radiosonde observations (marked as a red star in the top panel): daily maximum values in red; daily minimum values in blue; and moving average values for maximum, minimum, and 0.9, 0.75, and 0.5 quantiles are given by red, blue, orange, brown, and black lines, respectively. Climatology values are acquired from the SPC sounding climatology page (https://www.spc.noaa.gov/exper/soundingclimo).

greater than 45 dBZ and K_{DP} greater than $0.1°$ km^{-1}, rainfall rate R (in mm h^{-1}) is estimated as

$$R = a \times K_{DP}^b. \tag{5}$$

For the power law parameters, we take $a = 40.5$ and $b = 0.85$ (Chaney et al. 2022). If the two conditions above do not both hold, rainfall rate is estimated using a Z–R relationship:

$$R = \alpha \times Z^\beta, \tag{6}$$

where Z is in linear units (mm^6 m^{-3}), $\alpha = 0.017$, and $\beta = 0.71$ (see Fulton et al. 1998). The K_{DP} plays an important role in extreme rainfall estimation because of the prevalence of hail, which adversely affects rainfall estimates based on reflectivity and differential reflectivity fields (Giangrande and Ryzhkov 2008; Ryzhkov et al. 2022). For the periods of extreme rainfall, the operational hydrometeor classification (Giangrande and Ryzhkov 2008) included hail for both the Sterling, VA, and Fort Dix, NJ, radars.
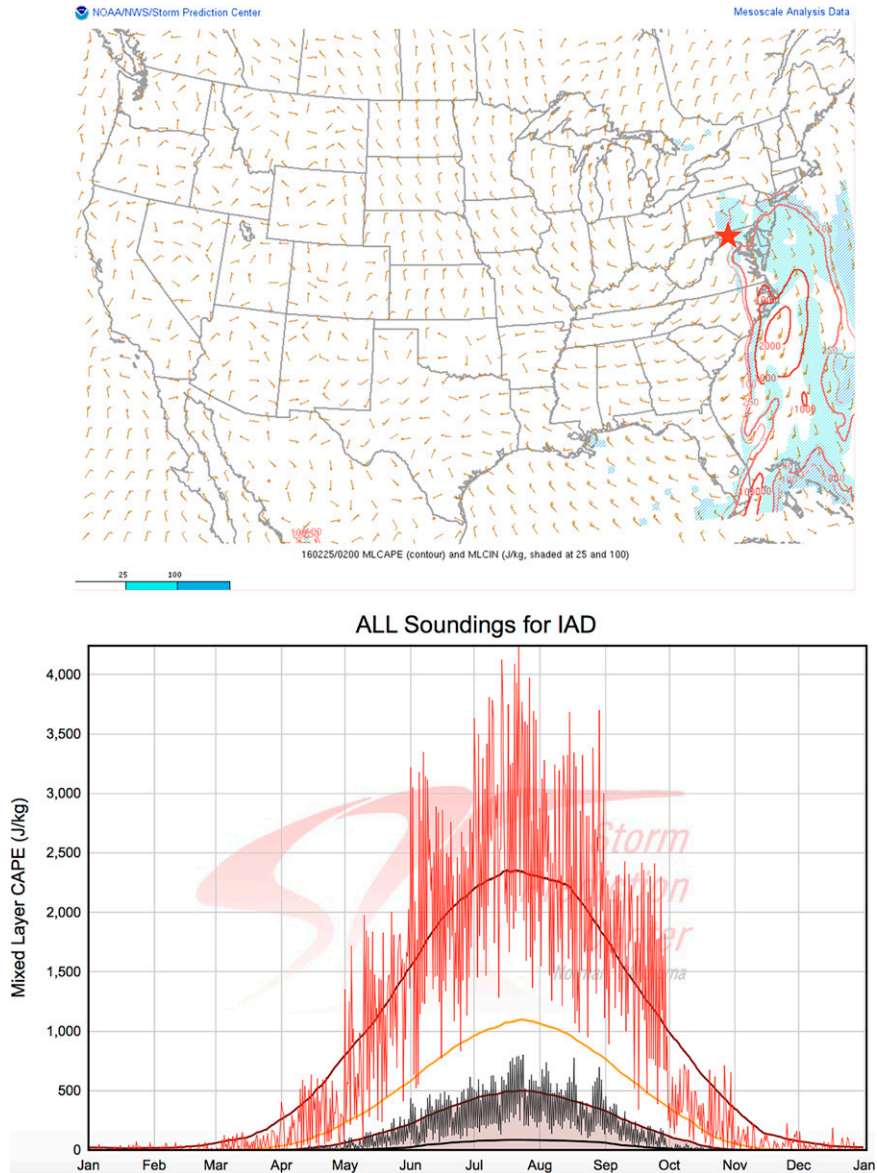
FIG. 6. (top) CAPE field from Storm Prediction Center at 0200 UTC 25 Feb. (bottom) The climatology of CAPE from Sterling, VA, radiosonde observations (marked as red star in top panel): daily maximum values in red and moving average values for maximum and 0.9, 0.75, and 0.5 quantiles are given by red, orange, brown, and black lines, respectively.

Regional analyses of rainfall over the eastern United States are based on the Stage IV radar rainfall fields developed by the National Weather Service. The spatial resolution of these rainfall fields is approximately 4 km and the time resolution is hourly (Lin and Mitchell 2005). The Stage IV dataset has been increasingly used for hydroclimatological analyses of rainfall extremes (Nelson et al. 2016; Ghebreyesus and Sharif 2021).

We identify supercells through local maxima in azimuthal shear fields computed from radar-derived Doppler velocity measurements using the SPORK-SPIN algorithms (Wilson et al. 2020; Van Den Broeke 2021; Wilson and Van Den Broeke 2021). We use an azimuthal shear threshold of $1.0 \text{ m s}^{-1} \text{ km}^{-1}$ for identifying mesocyclones. For additional details on mesocyclone detection, see Smith et al. (2016).

3. February 2016 storm

A powerful extratropical cyclone with upper level low moving north through the Great Lakes region combined with its associated frontal boundaries to produce severe thunderstorms, heavy rain and flash flooding over the eastern United
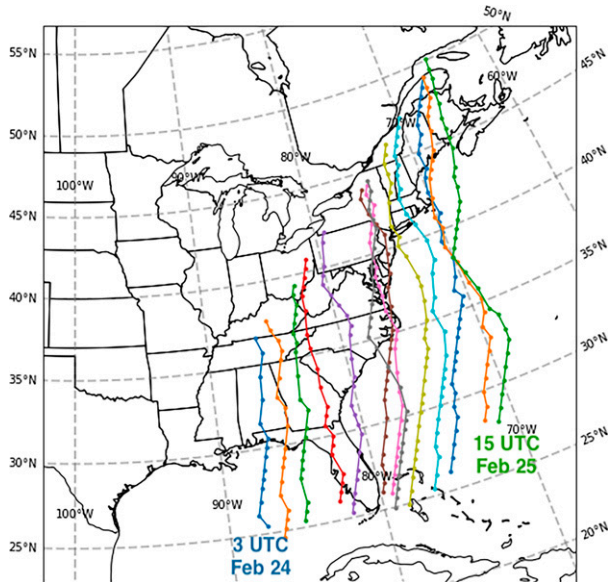
FIG. 7. The 3-hourly track position of the west-to-east-moving AR from 0300 UTC 24 Feb to 1500 UTC 25 Feb.

States on 24/25 February 2016. Heavy rainfall occurred over much of the eastern United States (Fig. 1), with regions of peak rainfall accumulations (50–125 mm) producing flash flooding. The storm produced more than 25 tornadoes from

North Carolina into Pennsylvania, with an EF3 tornado in northern Virginia and EF2 tornado in eastern Pennsylvania (https://www.spc.noaa.gov/exper/archive/events/).

a. Storm environment

The synoptic-scale environment of the storm during the period of peak rainfall in the Mid-Atlantic region was characterized by a closed low over the southern Great Lakes region at 500 hPa and a jet streak at 250 hPa (Fig. 2). The 500-hPa winds over Maryland and New Jersey were oriented from southwest to northeast with speeds in excess of 40 m s^{-1}. The left exit region of the jet streak—which provides support for upward vertical motion—was aligned with the region of heavy rainfall from Virginia through eastern Pennsylvania and New Jersey (Uccellini and Johnson 1979; Rose et al. 2004; Archambault et al. 2008).

At 2100 UTC 24 February, the surface low was located over Indiana, with a cold front extending southward through the Mid-Atlantic and southern United States (Fig. 3, top). A warm front, which was moving in a north-northeast direction, extended southward from central New Jersey through eastern Pennsylvania into northern Virginia. At 0300 UTC 25 February, the warm front extended through eastern Pennsylvania into lower New York (Fig. 3, bottom). In the Mid-Atlantic region, the cold front extended from central Pennsylvania through Virginia and was located just west of the Washington, D.C., region.
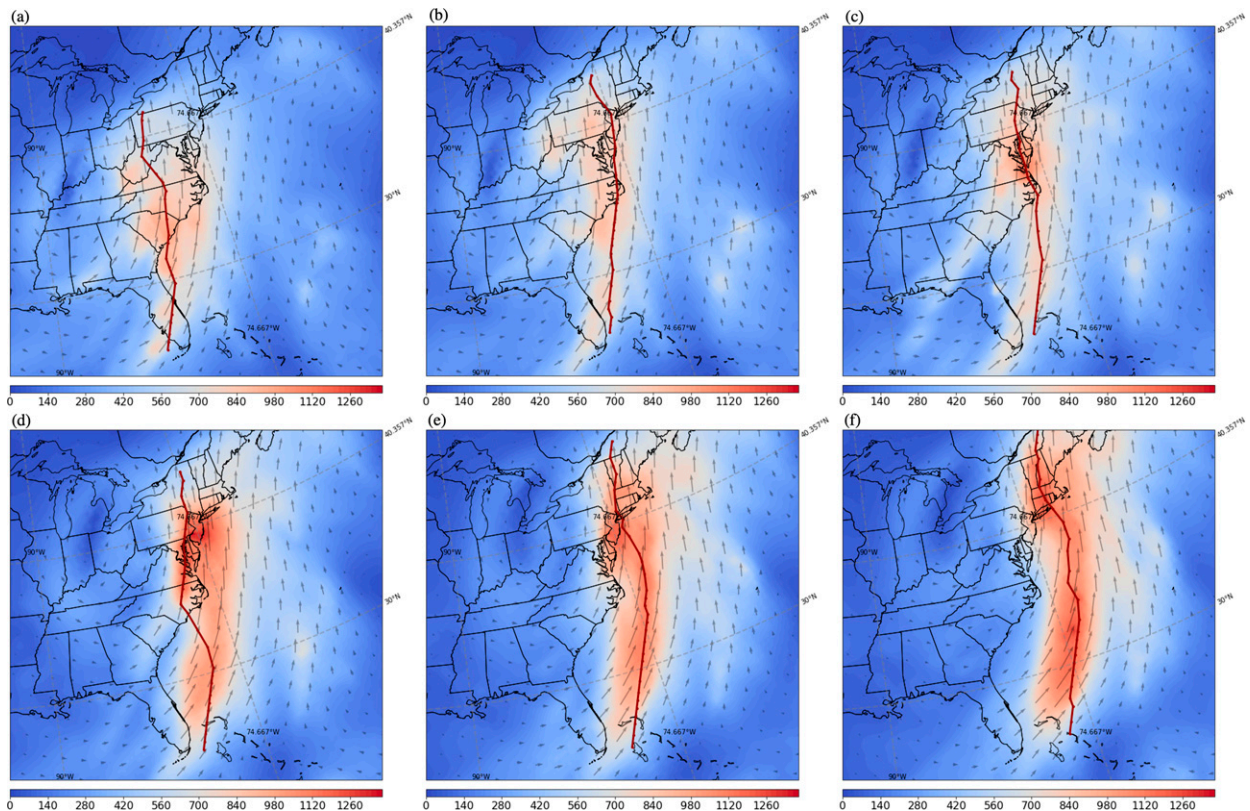

FIG. 8. Maps of 3-hourly instantaneous IVT fields (kg s^{-1} m^{-1}) computed from NARR, from 1500 UTC 24 Feb to 0600 UTC 25 Feb. The red dotted lines indicate the AR track position. Wind barb lengths are normalized using column-integrated wind.
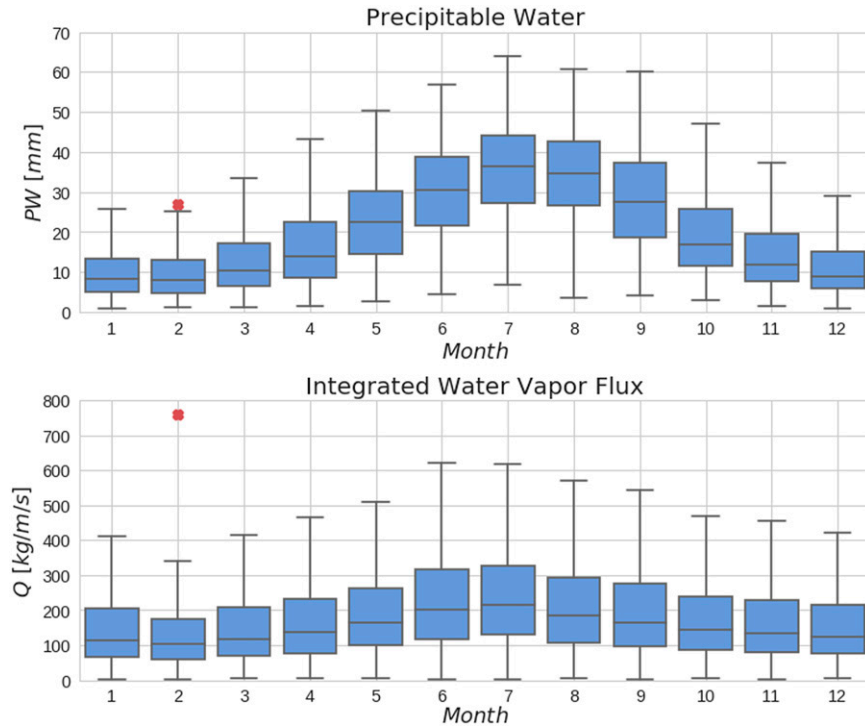
FIG. 9. Monthly boxplots of (top) precipitable water and (bottom) IVT from radiosonde observations from the Sterling, Virginia, radiosonde location. Upper and lower bounds of the blue boxes represent the 25th and 75th percentiles of the monthly data points; the top and bottom whiskers represent the 5th and 95th percentiles of the monthly data points. The values for 24 Feb 2016 are denoted by red symbols.

A low-level jet ahead of the cold front, coupled with subtropical moisture, resulted in strong water vapor transport to the Mid-Atlantic region at 850 hPa (Fig. 4, top). Comparably strong warm air advection occurred at 850 hPa (Fig. 4, bottom).

Wind shear, a key ingredient of supercells, was available in abundance. Storm relative helicity in the lowest 1 km of the atmosphere exceeded 500 $m^2 s^{-2}$ along an extensive south–north region extending through the Mid-Atlantic (Fig. 5, top), with peak values approaching 800 $m^2 s^{-2}$. Values larger than 100 $m^2 s^{-2}$ indicate the potential for tornadic supercells. The 0–6-km wind shear exceeded 35 m s^{-1} over the Mid-Atlantic with peak values greater than 50 m s^{-1} (figure not shown). Helicity and shear values were large, but not unprecedented for February in the Mid-Atlantic (Fig. 5).

It is rare to have positive convective available potential energy (CAPE) values during February in the Mid-Atlantic (Fig. 6, bottom), but they occurred over the Mid-Atlantic on 24 February. Mixed layer CAPE values exceeded 250 J kg^{-1} (Fig. 6, top). Maximum unstable CAPE (MUCAPE) values approached 1000 J kg^{-1} (Storm Prediction Center). Elevated CAPE values provide a distinctive feature of the extreme rainfall environment for the 24/25 February 2016 storms. The AR environment routinely provides some of the ingredients for supercells; CAPE is, however, often a missing ingredient for supercells in winter season ARs of

the northeastern United States. Positive, but small values of CAPE have been associated with extreme rainfall from ARs in California (Oakley et al. 2017; Huang et al. 2020).

b. Atmospheric rivers and atmospheric water balance extremes

The 24/25 February 2016 storm was associated with an AR episode that extended from 0300 UTC 24 February to 1500 UTC 25 February (Fig. 7). The first AR time period shows a south-to-north oriented line extending from the Gulf of Mexico through western Florida and Alabama into Tennessee. The AR maintained its south-to-north orientation while moving in the northeastward direction, matching the motion of the cold front. During the period of peak rainfall from 1800 UTC 24 February to 0600 UTC 25 February, the northern end of the AR remained nearly stationary over the Mid-Atlantic region, as shown in Fig. 8.

During the period from 23 to 25 February, IVT values over the Mid-Atlantic region increased steadily (Fig. 8). Peak values of IVT exceeded 1200 kg s^{-1} m^{-1} in New Jersey at 0000 UTC 25 February. The time of peak IVT in New Jersey immediately preceded peak rainfall over New Jersey from a long-duration supercell (as detailed below).

The seasonal distributions of precipitable water and IVT are illustrated in Fig. 9 through monthly boxplots derived from
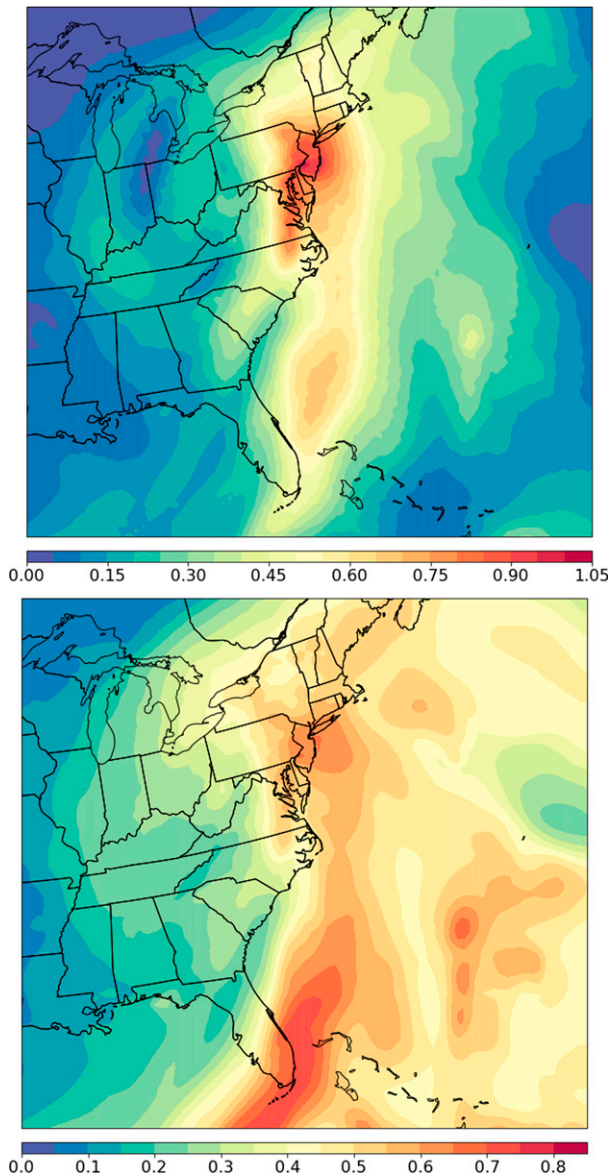
FIG. 10. Instantaneous anomaly fields of IVT for (top) 0000 and (bottom) 0300 UTC 25 Feb.

radiosonde observations at Sterling, Virginia. Maximum values of precipitable water (28 mm) and IVT (780 kg s^{-1} m^{-1}) at the Sterling, VA, radiosonde site for the February 2016 storm were anomalously high for the month of February. The precipitable water value, although above the 75th percentile for the month of February, was not as high as the average precipitable water during summer months (Fig. 9, top). The event-maximum IVT value, however, exceeded both February norms as well as the norms of summer months (Fig. 9, bottom). The value was also the maximum recorded at the station for the year 2016. Radiosonde data are acquired from the publicly available repository of the University of Wyoming (http://weather.uwyo.edu/upperair/sounding.html).
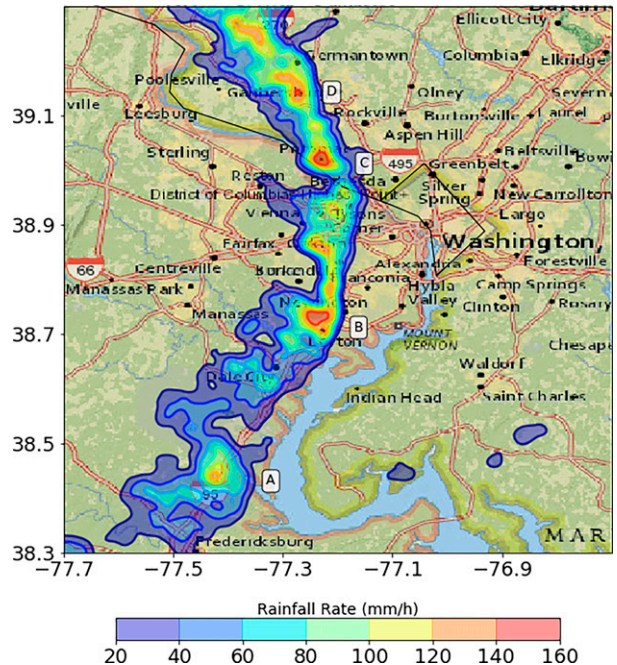

FIG. 11. Rain rate field at 2245 UTC 24 Feb, based on polarimetric rainfall estimates from the Sterling, VA, WSR-88D. Supercells (see Table 1) are identified by the labels A, B, C, and D.

Anomaly maps for IVT at 0000 and 0300 UTC 25 February illustrate the exceptional nature of water vapor transport for the February 2016 storm (Fig. 10). Anomaly maps are computed as the ratio of instantaneous IVT fields to the 10-yr return period fields (see section 2). Peak values of IVT at 0000 UTC exceeded 10-yr return interval values over New Jersey. The anomaly in precipitable water fields over the Princeton region were between 0.65 and 0.7 (figure not shown).

c. Extreme rainfall

Extreme rainfall in the Mid-Atlantic region from northern Virginia to New Jersey on 24/25 February 2016 was associated with supercells and storms with embedded mesovortices (a detailed summary of the severe weather outbreak is provided in the Storm Prediction Center's Severe Weather Events Archive; https://www.spc.noaa.gov/exper/archive/events/). Structure, motion, and evolution of storm elements dictated the locations of extreme rainfall and flooding in the Mid-Atlantic. Extreme rainfall was associated with both long-lived supercells (Bunkers et al. 2006; Davenport 2021) and clusters of supercells (Knupp et al. 2014).

A broken line of supercells developed in northern Virginia and Maryland during the afternoon and evening of 24 February (Fig. 11; see also the dashed red line in Fig. 3 for the location of the line of storms, relative to frontal boundaries). Support for vertical motion in the left exit region of the jet streak (Fig. 2), along with destabilization of the lower atmosphere by warm air advection (Fig. 4) contributed to the organization of supercells in the warm sector ahead of the cold front and south of the warm front.

TABLE 1. Storm speed, storm direction, maximum K_{DP}, and maximum rotation at 1 and 3 km for supercells identified in Fig. 11.

Label	Storm speed (m s^{-1})	Storm direction (°)	Max K_{DP} (° km^{-1})	Max rotation at 1 km (m s^{-1} km^{-1})	Max rotation at 3 km (m s^{-1} km^{-1})
A	22.0	222	4.0	2.4	4.3
B	25.4	215	7.4	4.0	4.5
C	25.0	220	6.6	3.6	2.3
D	25.2	214	5.8	2.5	4.7

Four supercells in northern Virginia and Maryland are identified through mesocyclone signatures at 2245 UTC 24 February (locations are denoted by the letters A, B, C, and D in Fig. 11). Each of the supercells exhibits strong rotation at 1 and 3 km (Table 1). Peak values of rotation range from 2.4 to 4.0 m s^{-1} km^{-1} at 1 km and from 2.3 to 4.7 m s^{-1} km^{-1} [see Smith et al. (2016) for related analyses of azimuthal shear in severe weather settings].
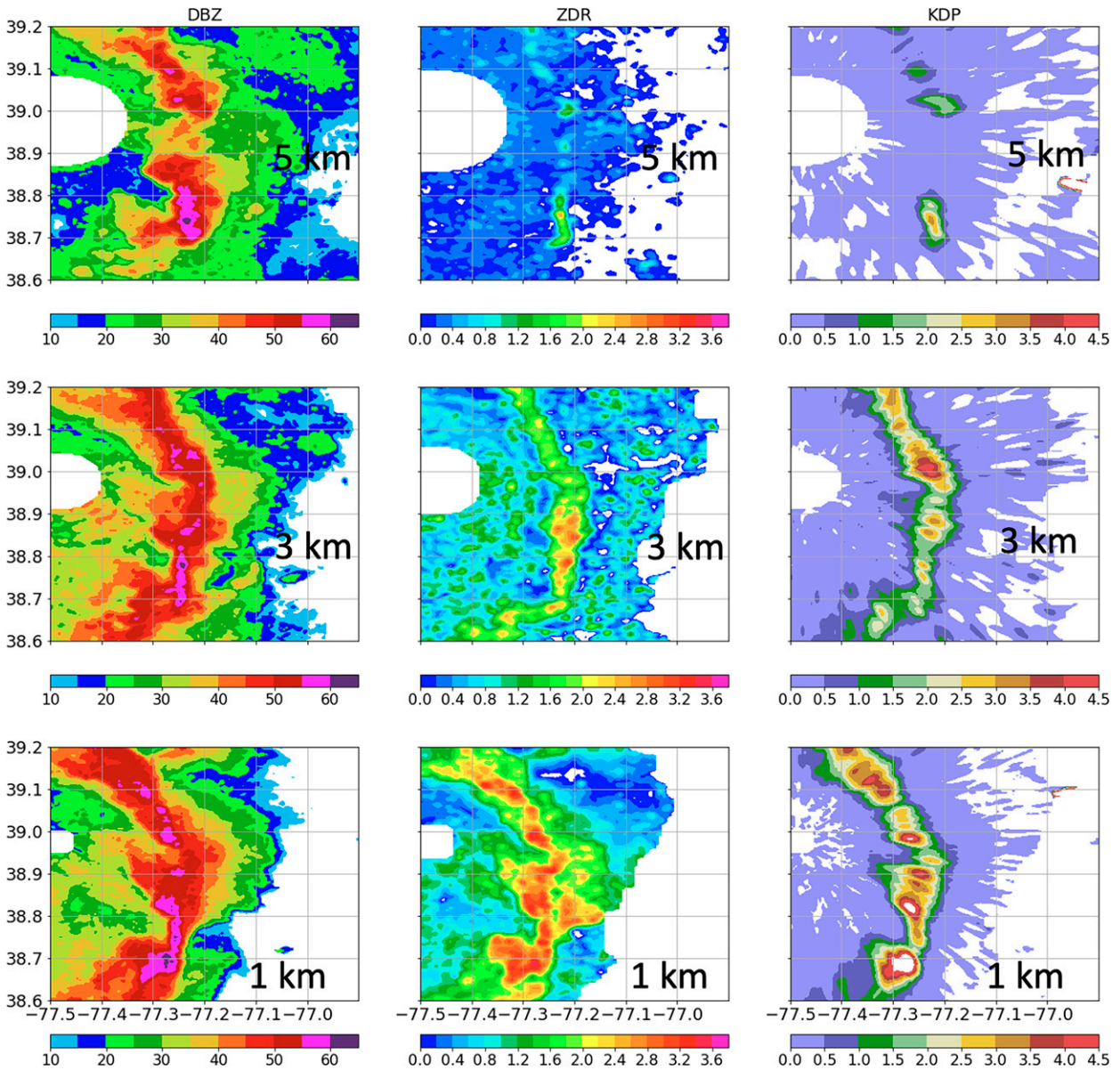

FIG. 12. (left) Reflectivity, (center) differential reflectivity, and (right) specific differential phase shift column at (top) 5-, (middle) 3-, and (bottom) 1-km elevation for 2245 UTC 24 Feb (KLWX radar).
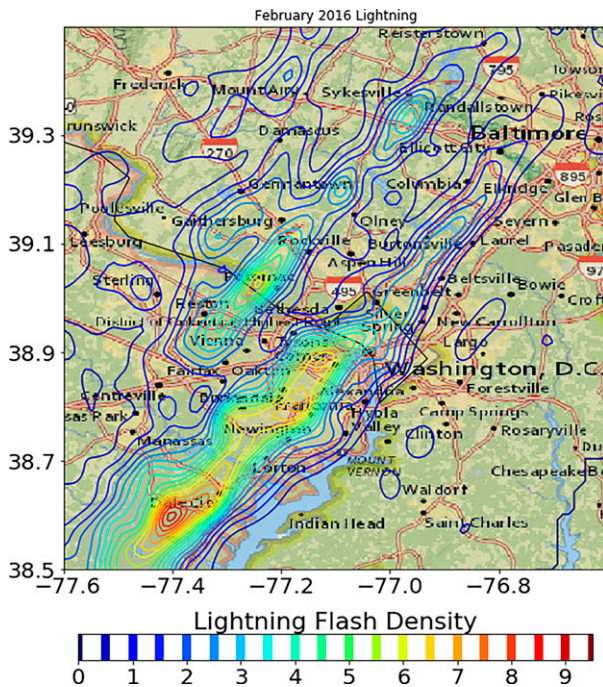
FIG. 13. Intracloud lightning flash density (strikes km^{-2}) for 24 Feb 2016 from National Lightning Detection Network observations.

Mean storm speed over the life cycle of the individual supercells ranges from 22 to 25 m s^{-1} (Table 1). Storm motion is from southwest to northeast, with mean values ranging from 214° to 222°. Storm speed and direction match the 500-hPa winds over northern Virginia (Fig. 2).

Paired with each supercell is a large region of extreme rainfall rates, as determined from the K_{DP} rainfall rate fields. A low-level K_{DP} feature, termed the K_{DP} foot by Romine et al. (2008), is often found in supercells, typically downshear of the mesocyclone and associated with the forward flank downdraft of the supercell. For each of the four supercells, area of the

K_{DP} foot (defined by a K_{DP} threshold of 1.5° km^{-1}; Fig. 12) exceeds 100 km^2 at some point in the storm life cycle. Peak values of K_{DP} exceed 7° km^{-1}, corresponding to rain rates greater than 200 mm h^{-1}.

The line of supercells produced extreme storm total lighting flash densities for the month of February (Fig. 13); intracloud flash densities exceeded 7 strikes km^{-2}. Vertical profiles of reflectivity, differential reflectivity and K_{DP} also point to anomalously strong convective intensity for storms during the month of February (Fig. 12). Regions of elevated Z_{DR} extending to 5 km, termed Z_{DR} columns (Kumjian 2013), indicate large, strong updrafts in the supercells. There were numerous reports of wind damage in the Washington metropolitan region during the period of peak rainfall rates (as detailed in the Storm Prediction Center's Severe Weather Events Archive). Significant wind damage in the northeastern United States has been associated with "collapsing K_{DP} columns" (Frugis 2020); more than 50% of the significant wind damage cases examined in Kuster et al. (2021) are classified as supercell events. In the cycle of mesocyclone growth and occlusion (Kumjian et al. 2010), collapsing K_{DP} columns may contribute to extreme short-duration rainfall extremes, in addition to damaging winds.

Supercells moved rapidly through urban watersheds in the Washington metropolitan area between 2245 and 2315 UTC producing large flood peaks at multiple USGS stream gauging stations. Despite the short duration of rainfall extremes and the partial coverage of the watershed by extreme rainfall, Cameron Run experienced a flood peak of 280 m³ s^{-1}— a 10-yr flood magnitude (Fig. 14). Record and near-record flooding occurred at USGS stream gauging stations along the Baltimore–Washington corridor.

The largest in situ rainfall rate measurements from the 24/25 February storm were in Princeton, NJ, where a Parsivel disdrometer recorded 1-min rainfall rates approaching 250 mm h^{-1} (Fig. 15). The time period of extreme rainfall rates at Princeton was less than 10 min; lightning and damaging winds accompanied peak rain rates. Rainfall rate
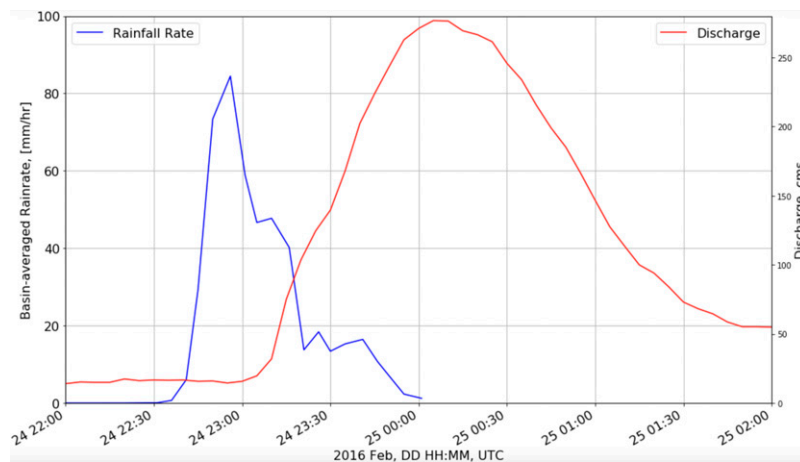

FIG. 14. Basin-average rainfall rate (mm h^{-1}) and discharge (m³ s^{-1}) time series for Cameron Run (USGS ID 01653000) on 24/25 Feb 2016.
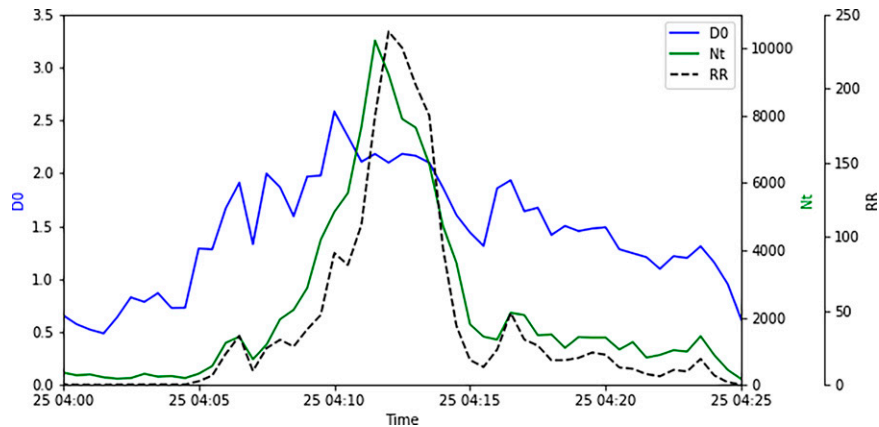
FIG. 15. Rainfall rate (RR), raindrop number density (Nt), and volume-weighted mean diameter (D0) for the period 0400–0425 UTC 25 Feb, based on disdrometer measurements in Princeton, NJ.

fields computed from polarimetric radar measurements at time resolution of 2.5 min illustrate striking variability of rainfall in time and space (Fig. 16). The location of the Princeton disdrometer is marked by a red star in each panel.

A long-lived supercell was responsible for the peak rainfall rates in Princeton. The storm element was large and moving at an exceptional speed. Storm area, as reflected in the size of the K_{DP} foot, i.e., the contiguous region with K_{DP} greater than $1.5°$ km^{-1}, exceeded 150 km^2 from 0340 to 0430 UTC. During this time, storm motion was to the northeast at speeds greater than 40 m s^{-1} (144 km h^{-1}); wind speeds at 500 hPa over central New Jersey were 40–44 m s^{-1} (Fig. 2). Rapid storm motion associated with strong steering winds is a key feature controlling the temporal and spatial variability of extreme rainfall.

During the period of peak rainfall in Princeton, extreme rainfall rates were located northwest of an elevated line of differential reflectivity at 1 km (Fig. 17). This "Z_{DR}" arc (Wilson and Van Den Broeke 2021) is associated with large drops, which are reflected in disdrometer measurements through a spike in rainfall-weighted median diameter before the rainfall rate peak (Fig. 15). The magnitude of Z_{DR} values in the arc feature are positively related to storm relative helicity (Kumjian and Ryzhkov 2009; Kumjian 2013). Downed trees and power lines were reported around the Princeton disdrometer location, pointing to strong downdrafts as ingredients of the extreme rainfall rate measurements.

The combined effect of rapid storm motion and storm size was to produce a 10-min period with intense convective rainfall across the Princeton region. The storm produced an annual maximum flood peak in the 115 km^2 Stony Brook watershed, despite only passing through a small portion of the watershed in approximately 15 min (a portion of the Stony Brook basin boundary is shown in Fig. 16).

Rotational motion was observed in the supercell from the time it entered southern New Jersey around 0330 UTC until it dissipated in northern New Jersey around 0445 UTC. Wind damage reports were also reported throughout New Jersey along the track of the supercell. The maximum azimuthal rotation rate at 3-km elevation was 11.9 m s^{-1} km^{-1} around the time of peak rain rates in Princeton at 0411 UTC. The maximum rotation rates at 1-km elevation were 3.4 m s^{-1} km^{-1} for the 0411 and 0416 UTC volume scans. Peak rainfall rates from the New Jersey supercell were linked to exceptionally strong rotation at 1- and 3-km elevations, anomalously large downdrafts—as reflected in wind damage reports, and a strong Z_{DR} arc signature.

Convective intensity, as represented by lightning flash density, peak reflectivity values, and echo tops for the New Jersey supercell, was weaker than for the Virginia supercells. Reflectivity values at the time of peak convective intensity for the New Jersey supercell reached 50 dBZ at 5-km elevation (Fig. 17), in contrast to the Virginia supercells, with reflectivity values greater than 65 dBZ at 5-km elevation (Fig. 12). Rotational motion for the New Jersey storm was comparable to or stronger than for the northern Virginia supercells. The cycle of mesocyclone spinup and occlusion likely contributes to the spatial and temporal variability of extreme rainfall rates (Smith et al. 2019). The relative importance of convective intensity and rotational motion in determining extreme rainfall rates warrants additional study, as does the role of extreme water vapor transport from ARs in sustaining extreme rain rates.

4. AR climatology

Given the importance of the AR in dictating extreme short-duration rainfall rates for the February 2016 storm, we examine the regional climatology of these storms. We created a 66-yr catalog of AR events that have occurred east of the Rocky Mountains based on 20CRV3 fields from 1950 to 2015.

Twelve ARs per year on average passed through the Princeton region (i.e., a $1° \times 1°$ domain centering on Princeton, NJ) (Fig. 18). The occurrence of ARs that pass through Princeton follows a clear seasonal cycle (Fig. 19), with a peak frequency
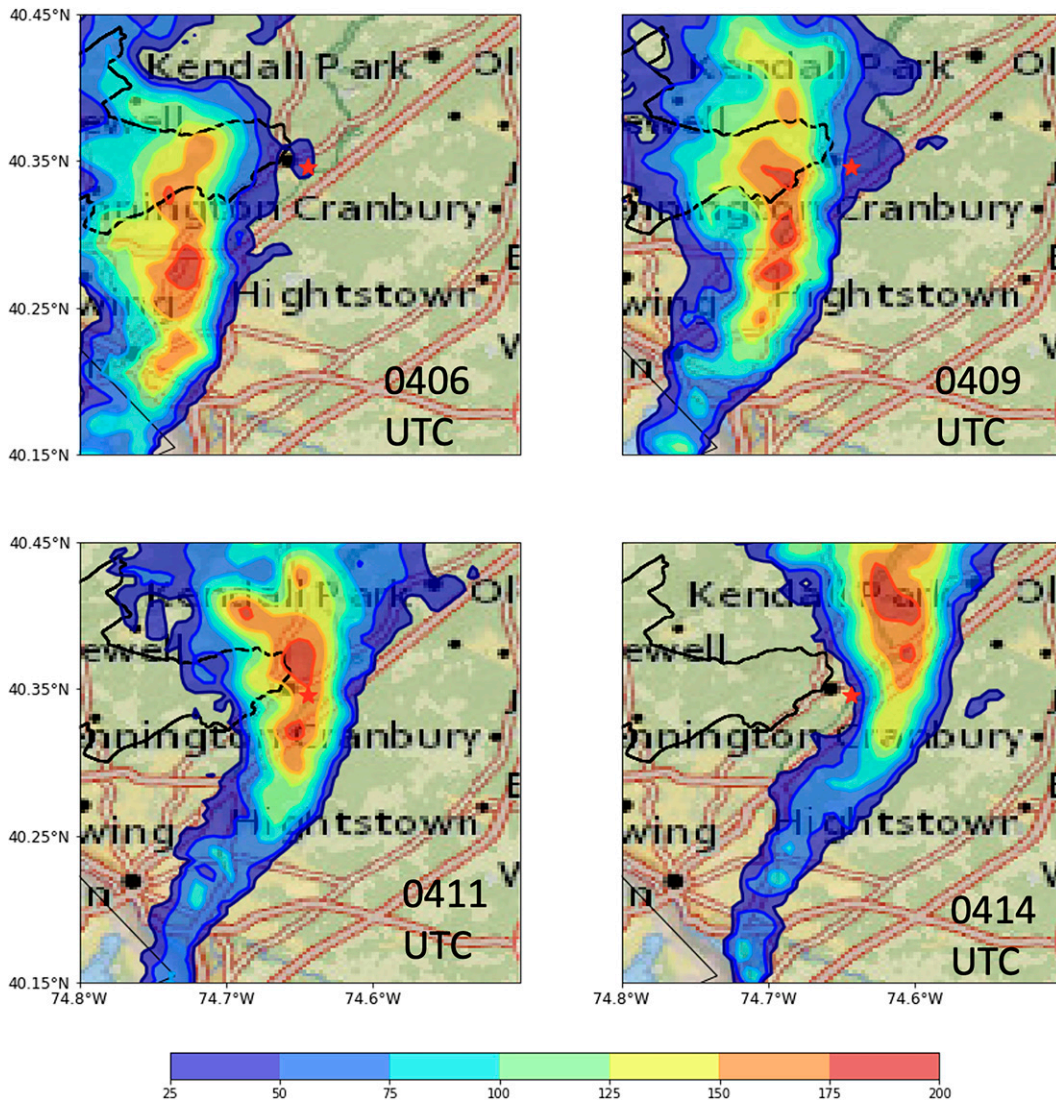
FIG. 16. Rainfall rate fields derived from polarimetric radar measurements (see text for details) at 0406, 0409, 0411, and 0414 UTC 25 Feb; the Princeton disdrometer is marked by a red star. The lower portion of the Stony Brook watershed is marked by a black line.

during November and December. Occurrence rates remain high from January to April but begin to decrease in May, reaching a minimum during the summer months (June–September). AR activity increases in frequency during October.

The spatial distribution of AR occurrence in the eastern United States (Fig. 20) shows the pronounced topographic effects of the Appalachian Mountains where AR activity is at a minimum. Peak AR activity takes place in the Lower Mississippi (Su et al. 2023). The seasonal cycle of AR occurrence (Fig. 21) is also characterized by large spatial gradients of AR frequency. Peak AR occurrence during the winter period from January to March extends from the Lower Mississippi River northeast into the Ohio River basin. Elevated frequency of ARs during the winter season is also found east of the Appalachians, with zone of maximum frequency

extending from the Carolinas through the Mid-Atlantic region. Similar features are found for the fall and early winter season, extending from October through December. The spring period from April through June has diminished frequency of ARs in the eastern United States, relative to the winter season.

Restricting the analyses to Princeton ARs, we observe that the near-coastal Atlantic has a local maximum and that peak IVT values in Princeton ARs tend to pass to the east of the Appalachian Mountains (Fig. 22). These ARs most frequently pass through the Chesapeake Bay area.

The Mann–Kendall test and Sen's slope estimator indicate a weak but statistically significant increasing trend in the annual count of ARs during the 66-yr period (i.e., 0.05 increase in count per year). The average AR lasts 39 h
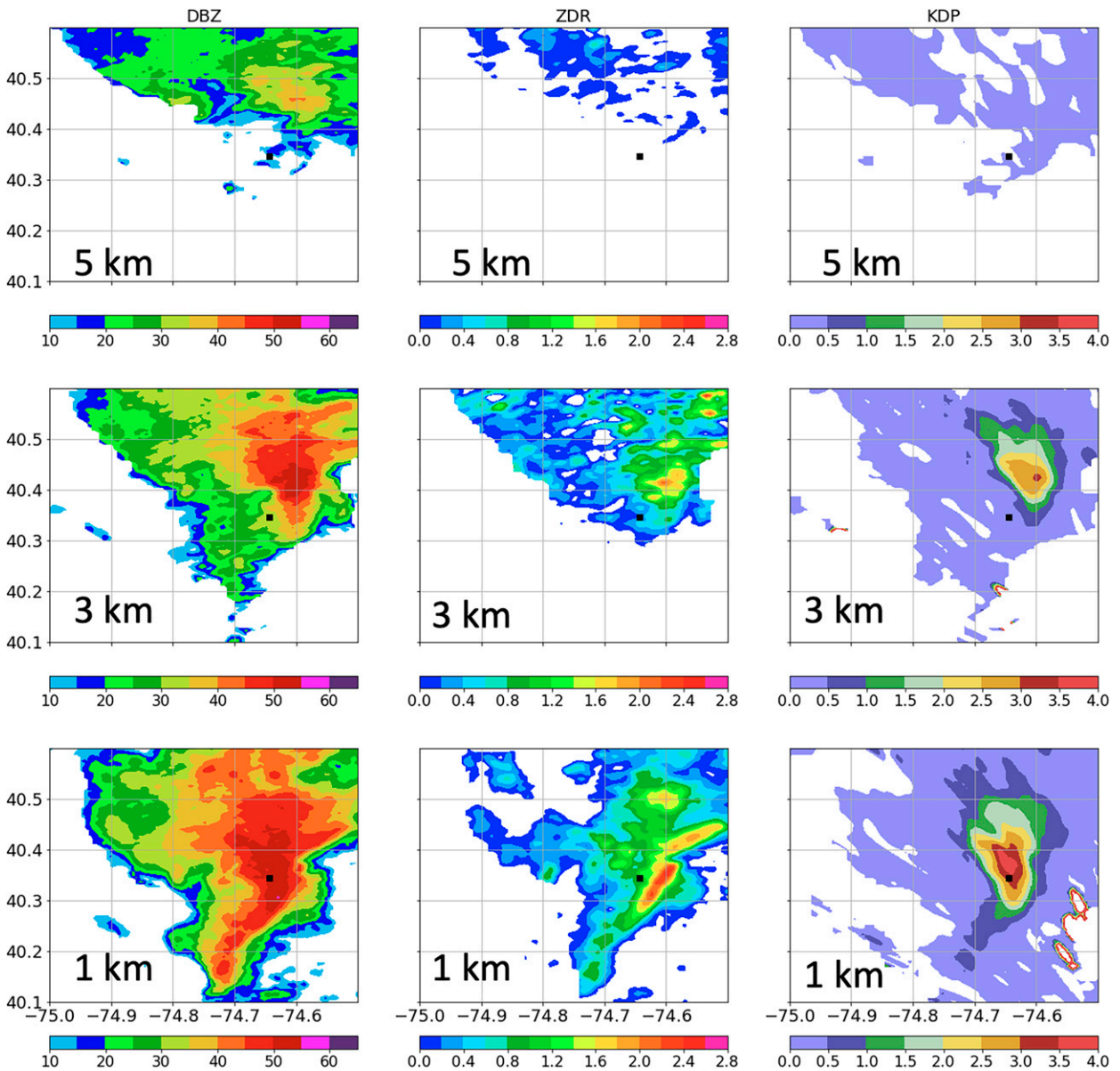
FIG. 17. (left) Reflectivity (dBZ), (center) differential reflectivity (dB), and (right) specific differential phase shift (° km^{-1}) at (top) -, (middle) 3-, and (bottom) 1-km elevation for 0416 UTC 25 Feb. Location of the Princeton disdrometer is marked by a black square.

and has a length of 1655 km, with maximum intensity of 1204 kg s^{-1} m^{-1}. No statistically significant evidence was found for long-term trends in the AR duration, length, or maximum intensity.

Lora et al. (2020) have found that AR frequency analyses show good agreement in extratropical regions across various AR detection algorithms. The increase in AR frequency is consistent with results from previous studies (Payne et al. 2020). Although the increased atmospheric moisture content and transport with warming can lead to intensification of extratropical cyclones, the reduction in baroclinic instability due to decreasing meridional temperature gradient (dynamical response

to warming) can lead to competing effects on extratropical cyclone and AR intensity (Payne et al. 2020). This may contribute to the absence of long-term trends in AR intensity from our 66-yr catalog. Payne et al. (2020) also suggest a poleward shift in ARs under warming, which can lead to increased exposure of the Mid-Atlantic region to ARs in the future. Further analysis of east coast AR climatology with a variety of detection algorithms will aid in a robust understanding of the east coast AR climatology.

The seasonality of ARs in the Mid-Atlantic region exhibits an extended period of elevated frequency during the winter season. Projected increases in CAPE during the winter season
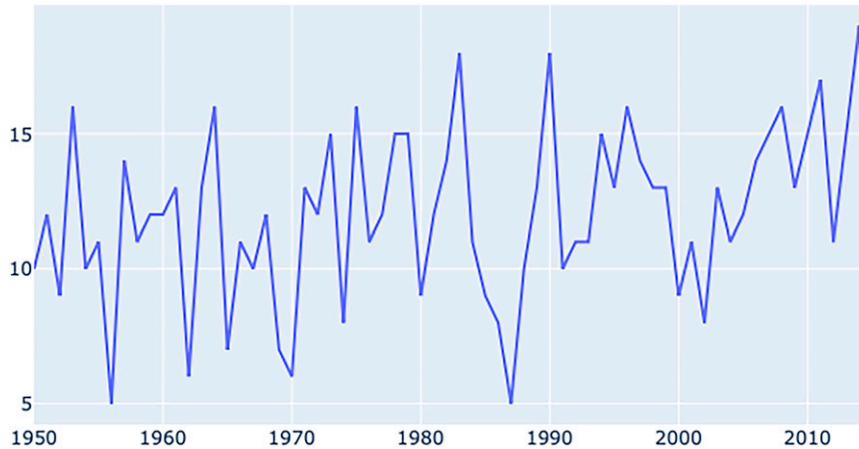
FIG. 18. Annual count of Princeton ARs from 1950 to 2015.

with climate change (Diffenbaugh et al. 2013) point to the potential for increasing frequency of subdaily rainfall extremes in a warming climate.

5. Discussion

Winter season flood peaks in the Mid-Atlantic reflect a mix of hydrometeorological and hydrologic processes (Smith et al. 2011b). In this section, we compare and contrast the diverse processes contributing to flooding from the February 2016 storm with those at play for major Mid-Atlantic floods in March 1936 and January 1996. Properties of ARs play a central role in comparing these major flood events. Winter season AR episodes in March 1936 and January 1996 produced record and near-record flooding in the Mid-Atlantic and northeastern United States (Fig. 23).

The St. Patrick's Day Storm of 17 March 1936 resulted in the record flood peak in the Potomac River from a stream gauging record of 125 years (Grover 1937; Miller 1990). The 19 January 1996 storm produced the fourth-largest flood peak in the Potomac River and record flooding at sites throughout the Susquehanna River basin (Barros and Kuligowski 1998; Grote 2021). As in February of 2016, extreme convective rainfall was a key ingredient of flooding in January 1996 and March 1936, as discussed below.

The seasonal distribution of flood peaks in the Potomac River exhibits a pronounced peak during late winter and early spring (Fig. 24), reflecting the role of land surface processes in controlling runoff production. Peak soil moisture during the late winter is tied to the seasonal cycle of evaporation. For some floods, including the March 1936 and January 1996 floods, snowmelt can contribute to flooding.
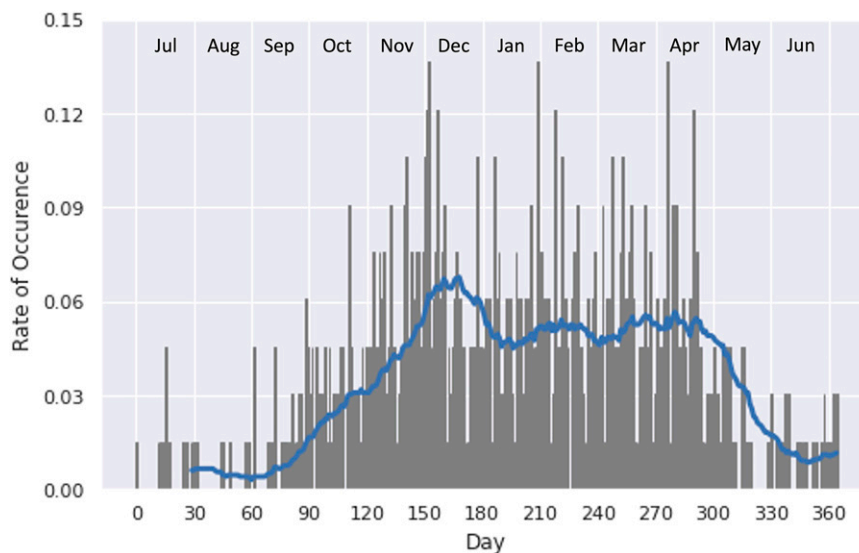

FIG. 19. Daily rate of occurrence (in gray bars) of Princeton ARs from 1950 to 2015, starting from 1 Jul. The blue line plots the moving 30-day average of the daily occurrence rate.
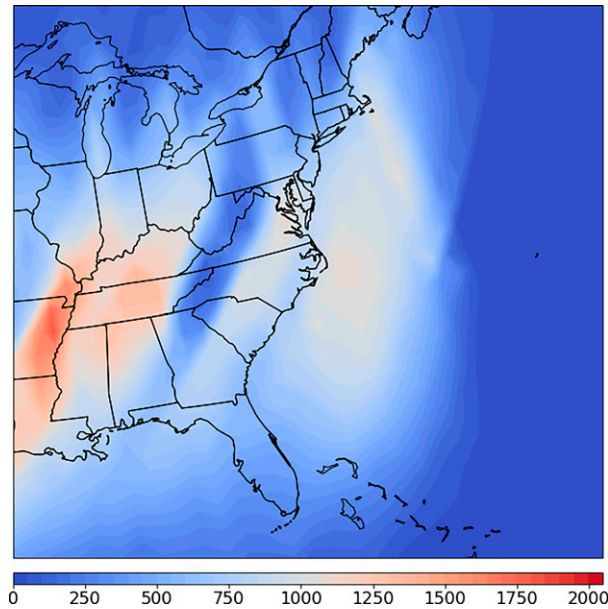
FIG. 20. Accumulated count of AR time steps from 1950 to 2015.

The March 1936 and January 1996 flood peaks were embedded in seasons with high frequency of AR episodes. In the 3 months preceding the 19 March 1936 flood peak in the Potomac River, eight major AR episodes passed through the region. Of particular importance was an AR episode on 10/11 March 1936 which delivered heavy rainfall and extensive snowpack to the Potomac River basin. Ten ARs passed through the Mid-Atlantic in the 3 months preceding the 21 January 1996 peak in the Potomac River, including two category-5 AR events earlier in January [see Ralph et al. (2019) for AR classification]. Extensive snowpack covered much of the Mid-Atlantic preceding the 19 January storm.

Like the earlier AR episodes during the fall and winter of 1995/96, the 19 January 1996 storm was a category-5 AR, with peak IVT of 1400 kg s^{-1} m^{-1}. It was an exceptionally long-duration (54 h) and extensive AR, with an average length of 2300 km. As the AR moved through the Mid-Atlantic, surface temperature increased rapidly from below freezing to more than 25°C. Rapid snowmelt contributed to extreme flooding in the Potomac, Susquehanna, and Delaware River basins. Paired with extreme water vapor flux in the AR was extreme warm air advection, a recipe for extreme flooding in settings with significant snowpack [see Guan et al. (2016) and Henn et al. (2020) for related analyses in the western United States].

Snowmelt was paired with extreme rainfall from the 19 January 1996 storm. The reflectivity field at 1504 UTC 19 January shows a line of intense convection that moved from west to east through the region (Fig. 25). Supercells embedded in the line of convection produced a tornado in northern Virginia; like the February 2016 storm, supercells were also agents of extreme, short-duration rainfall rates for the 19 January 1996 storm.

Snowmelt was not a major factor for the record flooding in the Potomac River during March of 1936. Although the AR episode in early March had produced significant snowpack in the watershed, warm temperatures had melted much of the snowpack before the St. Patrick's Day storm. On 17 March, only a small portion of the Blue Ridge region of the Potomac River basin was covered with snow (Grover 1937). Snowmelt from the earlier storm in March did not contribute directly to flood runoff and record flood peaks, but it did contribute to antecedent soil moisture preceding the 17 March storm. Rain and snowmelt from the preceding sequence of ARs contributed to soil moisture conditions that were likely close to saturation over much of the Potomac River basin (Grover 1937).

Surface observing stations along the path of the St. Patrick's Day storm reported extensive lightning on 17 March. Rain gauge observations from 17 March show accumulations of 100–150 mm over the Potomac River above the Point of Rocks gauging station (Grover 1937). Observational evidence suggests that extreme convective rainfall contributed to record flooding in the Potomac River.

We reconstructed the 1936 St. Patrick's Day storm using simulations from the Weather Research and Forecasting (WRF) Model, with initial and boundary conditions provided by Twentieth Century Reanalysis fields. Model implementation follows procedures used in Smith et al. (2011a). Results show a line of intense convection passing through the Potomac River basin (Fig. 26). The line of heavy rainfall was oriented from southwest to northeast and moved from west to east through the basin. The 1936 flood in the Potomac built from west to east to a record peak at Point of Rocks (Fig. 27). Structure, motion, and evolution of rainfall relative to the drainage network of the Potomac River contributed to the record flooding in the lower Potomac River.

Land surface processes tied to soil moisture and snowmelt contribute to the hydroclimatology of winter season flooding. If snow is present, strong warm air advection in ARs can result in rapid snowmelt and be a key ingredient of flood response. The sequence of ARs during the winter season plays an important role in determining antecedent moisture conditions. The combination of extreme convective rainfall and near-saturated soil moisture creates a recipe for record flooding, as was the case during March of 1936 in the Potomac River.

Assessing the changing flood regimes from winter season extratropical cyclones in a warming climate requires a balancing of competing factors. Climatological analyses of ARs in the previous section point to the potential for more frequent extratropical cyclones producing extreme water vapor transport—and heavy rainfall—over the Mid-Atlantic and northeastern United States. An atmospheric water balance perspective points to the potential for increasing flood peaks from winter season storms. Warming may decrease snowpack and soil moisture during the winter season. From a land surface water balance perspective, extremes of antecedent soil moisture—like those in March of 1936—and snowmelt—as in January of 1936—may occur less frequently. Climate model projections of snowpack and its connection to flooding have been extensively examined for the western United States, including links between ARs, snowpack
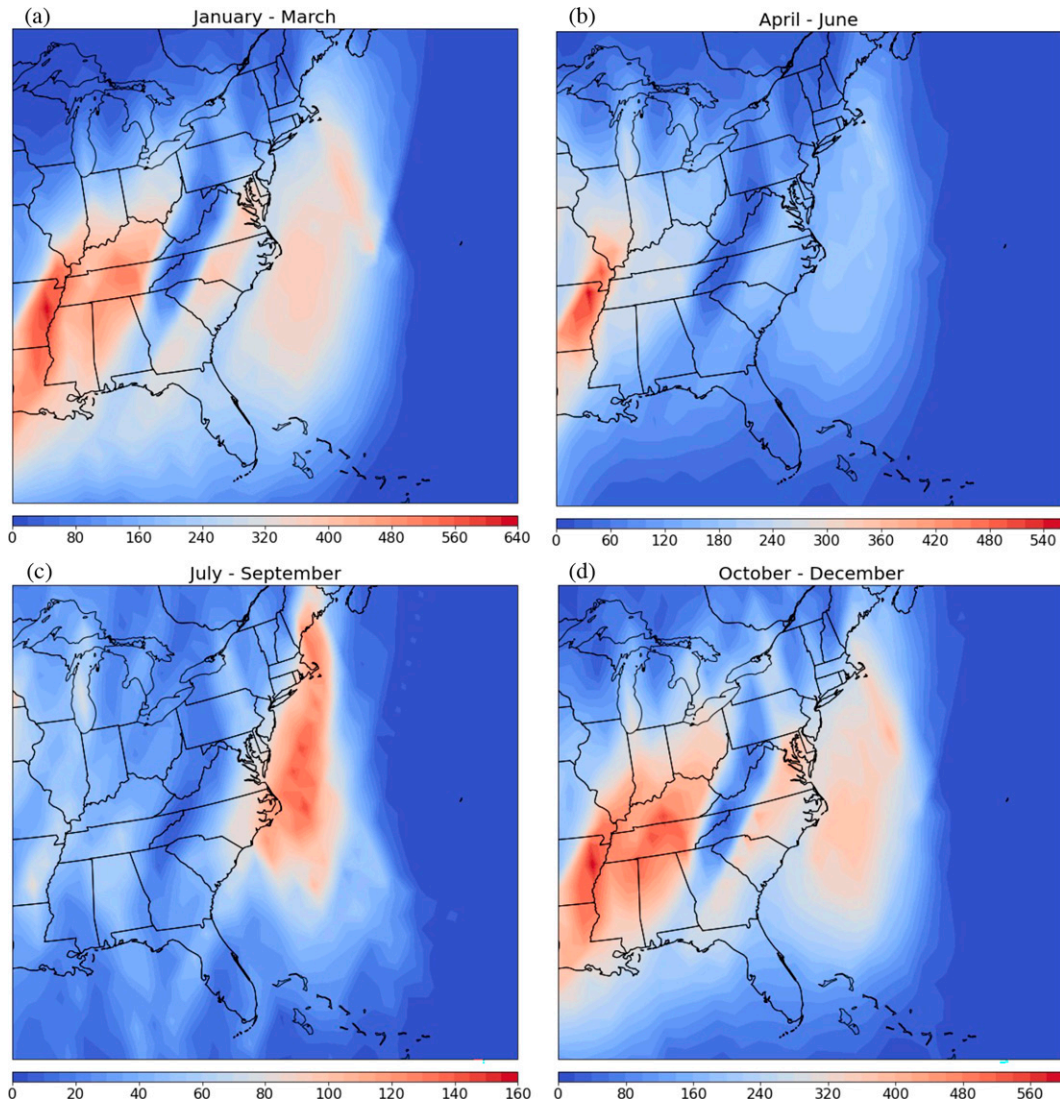
FIG. 21. Count of AR time steps from 1950 to 2015 for (a) January–March, (b) April–June, (c) July–September, and (d) October–December.

and flooding (e.g., Musselman et al. 2018). Less attention has been paid to snowpack and flooding in the eastern United States (e.g., Demaria et al. 2016).

A central question raised in this study is whether changing convective intensity will contribute to the evolving distribution of subdaily rainfall extremes during the winter season in the Mid-Atlantic and northeastern United States. Increases in short-duration rainfall extremes are found for settings, like northern Europe, in which stratiform precipitation is being supplanted by weak convective rain (Fowler et al. 2021). Do similar transitions occur across the convective intensity spectrum? Robust increases in CAPE and severe weather environments in the eastern United States have been identified in climate model studies (Diffenbaugh et al. 2013; Song et al. 2022). Increasing CAPE in the eastern United States is found during all seasons, including the

January–March period (Diffenbaugh et al. 2013). Climate change may increase the frequency of AR episodes, like the February 2016 system, in which elevated CAPE leads to extreme rainfall rates from organized convection and supercells.

The spatial structure and temporal evolution of extreme convective rainfall during the Winter season will play an important role in determining evolving flood hazards in the Mid-Atlantic and northeastern United States. As illustrated through analyses of the 24/25 February 2016 storm, rainfall from winter season extratropical cyclones can exhibit striking temporal and spatial variability, with peak rainfall rates that rival warm season convective systems. Rainfall variability is tied to convective organization, size, and motion of storm elements and peak rainfall rates from storm elements. Increases in convective intensity during winter
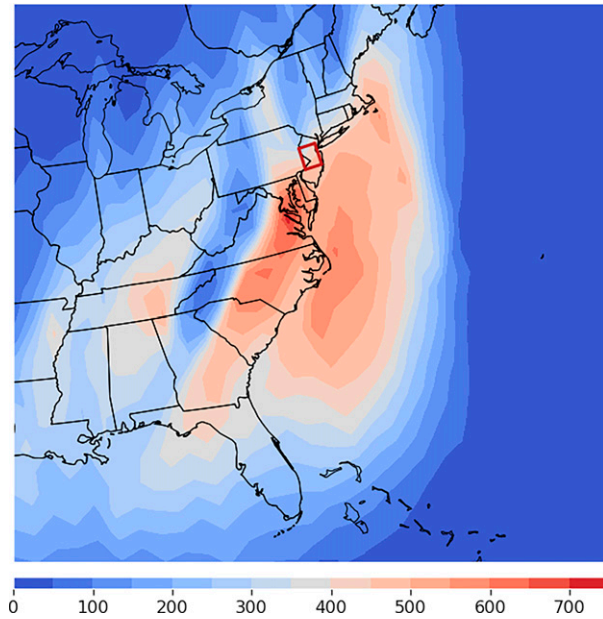
FIG. 22. Accumulated count of AR time steps for Princeton ARs from 1950 to 2015. The red box indicates the $1° \times 1°$ domain centering on Princeton, NJ.

season AR events—with the associated increases in peak short-duration rainfall rates—could have particularly large impacts on flood hazards in urban environments (Cristiano et al. 2017).

6. Summary and conclusions

In this study, we examined the role of winter season extratropical cyclones as flood agents in the Mid-Atlantic region of the United States. Principal conclusions are the following:

- A powerful extratropical cyclone produced extreme short-duration rainfall and flooding in the Mid-Atlantic region of the United States on 24/25 February 2016. Extreme rainfall was linked to a major AR episode, with near-record values of vertically integrated water vapor flux. Supercells were the agents of extreme rainfall and flooding, especially along the Washington–Baltimore corridor and in central New Jersey. Peak rainfall rates from disdrometer measurements in Princeton, New Jersey, approached 250 mm h^{-1}.
- Structure, motion and evolution of supercells contributed to extreme variability of rainfall in space and time. Storm speed was exceptional, especially for the long-duration supercell producing peak rainfall rates and flooding over central New Jersey; peak speeds exceeded 40 m s^{-1}, matching the 500-hPa winds. Storm size, i.e., the size of the extreme rain rate area from a supercell, also plays an important role in rainfall extremes. Convective intensity, as reflected in lightning flash density and echo tops, varied over the region, with stronger convection in the Baltimore–Washington region than in New Jersey. Rotational motion and peak rainfall rates from the
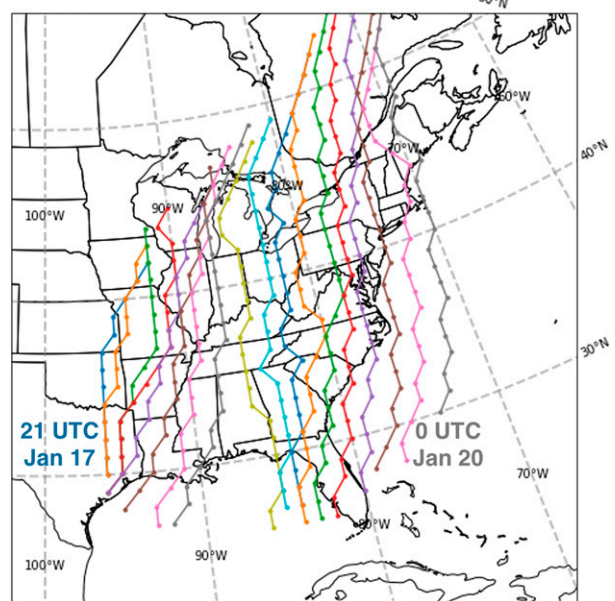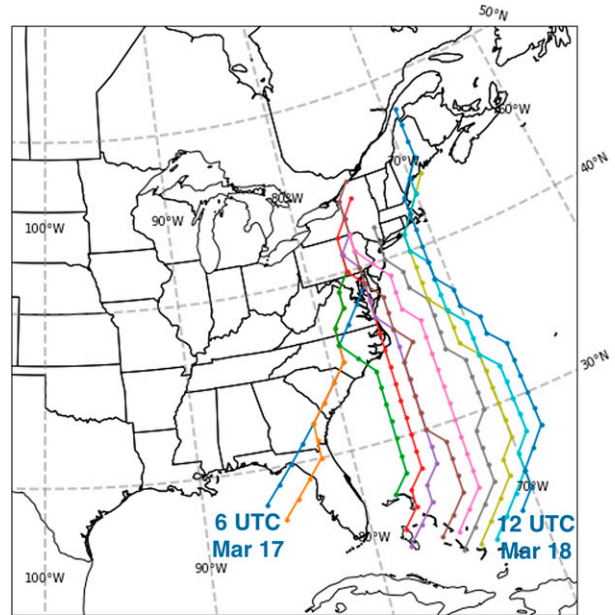

FIG. 23. The 3-hourly track position of the (top) west-to-east-moving AR from 0600 UTC 17 Mar to 1200 UTC 18 Mar 1936 and (bottom) west-to-east-moving AR from 2100 UTC 17 Jan to 0000 UTC 20 Jan 1996.

New Jersey supercell were, however, larger than for the more intense supercells in northern Virginia and Maryland.
- Extreme rainfall from the 24/25 February 2016 storm system was associated with an exceptionally strong AR, with peak magnitudes of vertically integrated water vapor flux exceeding 1250 kg s^{-1} m^{-1}, a category-5 AR based on the classification system of Ralph et al. (2019). Organization and evolution of convection was tied to a jet streak; the left exit region of the jet streak provided support for vertical motion. Transport of
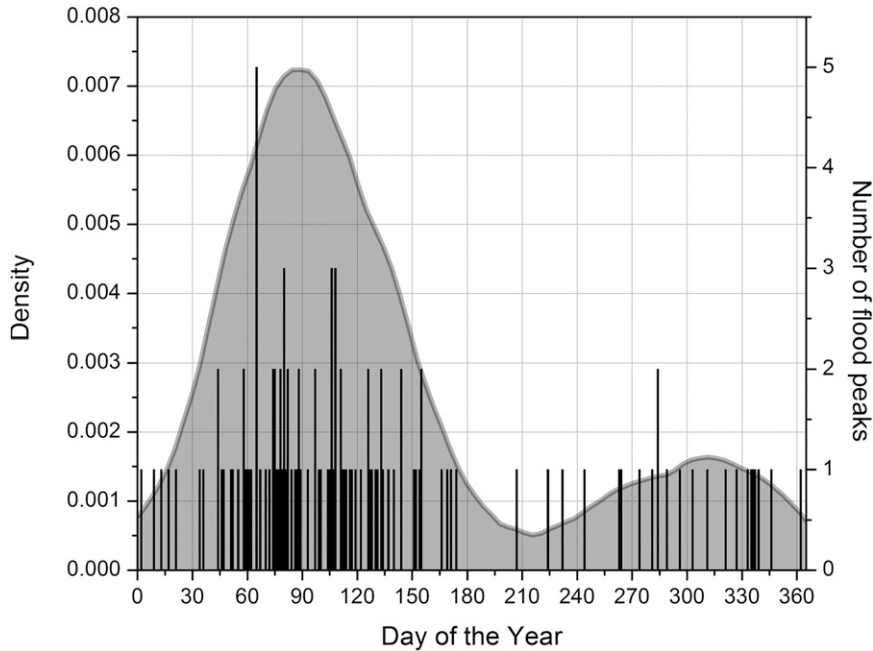
FIG. 24. Seasonal distribution (from January to December) of flood peaks in the Potomac River basin.

warm, moist air also contributed to destabilization and organization of convection.

- Storm-relative helicity and 0–6-km wind shear were large, but not unprecedented for the winter season in the Mid-Atlantic region. The element of storm environment that distinguished the 24/25 February 2016 storm was convective available potential energy (CAPE). Positive CAPE values are rare during the winter season, as reflected in the Sterling, Virginia, radiosonde climatology, but were an important ingredient of the 24/25 February 2016 storms.

- Climatological analyses of AR episodes in the Mid-Atlantic region exhibit pronounced spatial gradients, with peak occurrence rates near Chesapeake Bay. There is an extended period from late fall to early spring with elevated occurrence frequency of AR episodes. Analyses of the 66-yr AR dataset derived from Twentieth Century Reanalysis fields suggest that the frequency of these storms is increasing over the Mid-Atlantic region. An increase in AR frequency, combined with increasing frequency of elevated CAPE during the winter season over the Mid-Atlantic region, as well as the poleward shift in extratropical cyclones
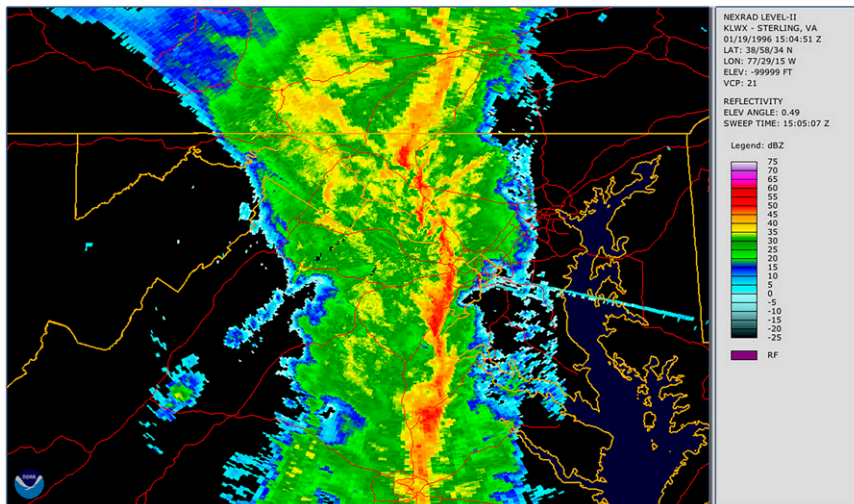

FIG. 25. Reflectivity field from the Sterling, VA, WSR-88D at 1504 UTC 19 Jan 1996.
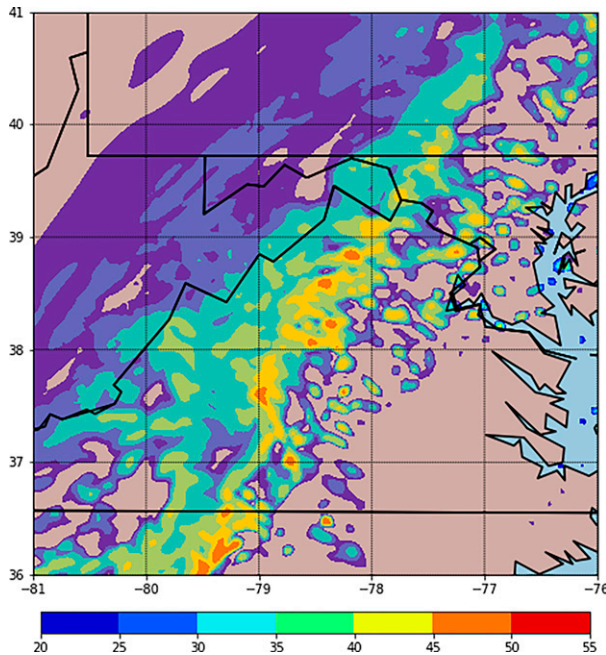
FIG. 26. WRF reflectivity field at 1000 UTC 17 Mar 1936.

under warming could result in pronounced changes to the climatology of extreme rainfall.

• Winter season extratropical cyclones in March 1936 and January 1996 produced record and near-record flooding in Mid-Atlantic rivers. The principal agents of extreme flooding in both cases were powerful AR episodes and the associated convective rainfall. The March 1936 flood event was preceded by eight AR episodes in the 3-month period prior to peak flooding; peak flooding in January 1996 was preceded by ten AR events in the prior 3 months. Changing properties of winter season extratropical cyclones in a warming climate will be paired with changes in land surface
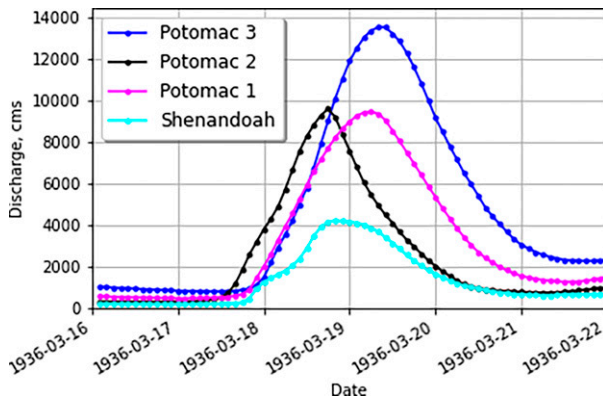

FIG. 27. Potomac River hydrographs for the March 1936 flood; Potomac 1 is for Potomac River at Hancock USGS ID 0161300), Potomac 2 is Potomac River at Shepherdstown (USGS ID 0161800), Potomac 3 is Potomac River at Point of Rocks (USGS ID 01638500), and Shenandoah is the for the Shenandoah River at Millville (USGS ID 01636500).

processes, with both contributing to the evolving flood regime.

REFERENCES

American Meteorological Society, 2022: Atmospheric river. Glossary of Meteorology, https://glossary.ametsoc.org/wiki/Atmospheric_river.

Archambault, H. M., L. F. Bosart, D. Keyser, and A. R. Aiyyer, 2008: Influence of large-scale flow regimes on cool-season precipitation in the northeastern United States. *Mon. Wea. Rev.*, **136**, 2945–2963, https://doi.org/10.1175/2007MWR2308.1.

Barros, A. P., and R. J. Kuligowski, 1998: Orographic effects during a severe wintertime rainstorm in the Appalachian Mountains. *Mon. Wea. Rev.*, **126**, 2648–2672, https://doi.org/10.1175/1520-0493(1998)126<2648:OEDASW>2.0.CO;2.

Bunkers, M. J., M. R. Hjelmfelt, and P. L. Smith, 2006: An observational examination of long-lived supercells. Part I: Characteristics, evolution, and demise. *Wea. Forecasting*, **21**, 673–688, https://doi.org/10.1175/WAF949.1.

Chandrasekar, V., V. N. Bringi, N. Balakrishnan, and D. S. Zrnić, 1990: Error structure of multiparameter radar and surface measurements of rainfall. Part III: Specific differential phase. *J. Atmos. Oceanic Technol.*, **7**, 621–629, https://doi.org/10.1175/1520-0426(1990)007<0621:ESOMRA>2.0.CO;2.

Chaney, M. M., J. A. Smith, and M. L. Baeck, 2022: Range dependence of polarimetric radar estimates for extreme flood-producing rainfall in urban watersheds. *J. Hydrometeor.*, **23**, 1205–1226, https://doi.org/10.1175/JHM-D-21-0191.1.

Compo, G. P., and Coauthors, 2011: The twentieth century reanalysis project. *Quart. J. Roy. Meteor. Soc.*, **137**, 1–28, https://doi.org/10.1002/qj.776.

Cristiano, E., M.-C. ten Veldhuis, and N. Van De Giesen, 2017: Spatial and temporal variability of rainfall and their effects on hydrological response in urban areas–A review. *Hydrol. Earth Syst. Sci.*, **21**, 3859–3878, https://doi.org/10.5194/hess-21-3859-2017.

Davenport, C. E., 2021: Environmental evolution of long-lived supercell thunderstorms in the Great Plains. *Wea. Forecasting*, **36**, 2187–2209, https://doi.org/10.1175/WAF-D-21-0042.1.

Demaria, E. M. C., J. K. Roundy, S. Wi, and R. N. Palmer, 2016: The effects of climate change on seasonal snowpack and the hydrology of the northeastern and upper midwest United States. *J. Climate*, **29**, 6527–6541, https://doi.org/10.1175/JCLI-D-15-0632.1.

Dettinger, M. D., F. M. Ralph, T. Das, P. J. Neiman, and D. R. Cayan, 2011: Atmospheric rivers, floods and the water resources of California. *Water*, **3**, 445–478, https://doi.org/10.3390/w3020445.

Diffenbaugh, N. S., M. Scherer, and R. J. Trapp, 2013: Robust increases in severe thunderstorm environments in response to greenhouse forcing. *Proc. Natl. Acad. Sci. USA*, **110**, 16 361–16 366, https://doi.org/10.1073/pnas.1307758110.

Doswell, C. A., III, H. E. Brooks, and R. A. Maddox, 1996: Flash flood forecasting: An ingredients-based methodology. *Wea. Forecasting*, **11**, 560–581, https://doi.org/10.1175/1520-0434(1996)011<0560:FFFAIB>2.0.CO;2.

Fowler, H. J., and Coauthors, 2021: Towards advancing scientific knowledge of climate change impacts on short-duration rainfall extremes. *Philos. Trans. Roy. Soc.*, **A379**, 20190542, https://doi.org/10.1098/rsta.2019.0542.

Frugis, B. J., 2020: The use of collapsing specific differential phase columns to predict significant severe thunderstorm wind damage across the northeastern United States. Eastern Region Tech. Attachment 2020-04, NOAA National Weather Service, 16 pp., https://www.weather.gov/media/erh/ta2020-04.pdf.

Fulton, R., J. P. Breidenbach, D.-J. Seo, D. A. Miller, and T. O'Bannon, 1998: The WSR-88D rainfall algorithm. *Wea. Forecasting*, **13**, 377–395, https://doi.org/10.1175/1520-0434(1998)013<0377:TWRA>2.0.CO;2.

Ghebreyesus, D. T., and H. O. Sharif, 2021: Development and assessment of high-resolution radar-based precipitation intensity-duration-curve (IDF) curves for the state of Texas. *Remote Sens.*, **13**, 2890, https://doi.org/10.3390/rs13152890.

Giangrande, S. E., and A. V. Ryzhkov, 2008: Estimation of rainfall based on the results of polarimetric echo classification. *J. Appl. Meteor. Climatol.*, **47**, 2445–2462, https://doi.org/10.1175/2008JAMC1753.1.

Grote, T., 2021: A synoptic climatology of rain-on-snow flooding in Mid-Atlantic region using NCEP/NCAR re-analysis. *Phys. Geogr.*, **42**, 452–471, https://doi.org/10.1080/02723646.2020.1838119.

Grover, N. C., 1937: The floods of 1936; Part 3: Potomac, James and upper Ohio Rivers. USGS Water Supply Paper 800, 381 pp., https://pubs.usgs.gov/wsp/0800/report.pdf.

Grumm, R. H., J. Ross, and P. Knight, 2005: Examining severe weather events using reanalysis datasets. *21st Conf. on Weather Analysis and Forecasting*, Washington, DC, Amer. Meteor. Soc., P1.87, https://ams.confex.com/ams/WAFNWP34BC/techprogram/paper_94351.htm.

Guan, B., and D. E. Waliser, 2015: Detection of atmospheric rivers: Evaluation and application of an algorithm for global studies. *J. Geophys. Res. Atmos.*, **120**, 12 514–12 535, https://doi.org/10.1002/2015JD024257.

——, ——, F. M. Ralph, E. J. Fetzer, and P. J. Neiman, 2016: Hydrometeorological characteristics of rain-on-snow events associated with atmospheric rivers. *Geophys. Res. Lett.*, **43**, 2964–2973, https://doi.org/10.1002/2016GL067978.

Helmus, J. J., and S. M. Collis, 2016: The Python ARM radar toolkit (Py-ART), a Library for working with weather radar data in the Python programming language. *J. Open Res. Software*, **4**, e25, https://doi.org/10.5334/jors.119.

Helsel, D. R., and R. M. Hirsch, 1993: *Statistical Methods in Water Resources*. 1st ed. Elsevier, 522 pp.

Henn, B., K. N. Musselman, L. Lestak, F. M. Ralph, and N. P. Molotch, 2020: Extreme runoff generation from atmospheric river driven snowmelt during the 2017 Oroville Dam spillways incident. *Geophys. Res. Lett.*, **47**, e2020GL088189, https://doi.org/10.1029/2020GL088189.

Huang, X., D. L. Swain, D. B. Walton, S. Stevenson, and A. D. Hall, 2020: Simulating and evaluating atmospheric river-induced precipitation extremes along the US Pacific Coast: Case studies from 1980–2017. *J. Geophys. Res. Atmos.*, **125**, e2019JD031554, https://doi.org/10.1029/2019JD031554.

Kingfield, D. M., and M. M. French, 2022: The influence of WSR-88D intra-volume scanning strategies on thunderstorm observations and warnings in the dual-polarization radar era: 2011–20. *Wea. Forecasting*, **37**, 283–301, https://doi.org/10.1175/WAF-D-21-0127.1.

Knupp, K. R., and Coauthors, 2014: Meteorological overview of the devastating 27 April 2011 tornado outbreak. *Bull. Amer. Meteor. Soc.*, **95**, 1041–1062, https://doi.org/10.1175/BAMS-D-11-00229.1.

Kumjian, M. R., 2013: Principles and applications of dual-polarization radar. *J. Oper. Meteor.*, **1**, 226–274, http://dx.doi.org/10.15191/nwajom.2013.0119.

——, and A. V. Ryzhkov, 2009: Storm-relative helicity revealed from polarimetric radar measurements. *J. Atmos. Sci.*, **66**, 667–685, https://doi.org/10.1175/2008JAS2815.1.

——, ——, V. M. Melnikov, and T. J. Schuur, 2010: Rapid-scan super-resolution observations of a cyclic supercell with a dual-polarization WSR-88D. *Mon. Wea. Rev.*, **138**, 3762–3786, https://doi.org/10.1175/2010MWR3322.1.

Kunkel, K. E., D. R. Easterling, D. A. R. Kristovich, B. Gleason, L. Stoecker, and R. Smith, 2012: Meteorological causes of the secular variations in observed extreme precipitation for the conterminous United States. *J. Hydrometeor.*, **13**, 1131–1141, https://doi.org/10.1175/JHM-D-11-0108.1.

Kuster, C. M., B. R. Bowers, J. T. Carlin, T. J. Schuur, J. W. Brogden, R. Toomey, and A. Dean, 2021: Using K_{DP} cores as a downburst precursor signature. *Wea. Forecasting*, **36**, 1183–1198, https://doi.org/10.1175/WAF-D-21-0005.1.

Lang, T. J., D. A. Ahijevych, S. W. Nesbitt, R. E. Carbone, S. A. Rutledge, and R. Cifelli, 2007: Radar-observed characteristics of precipitating systems during NAME 2004. *J. Climate*, **20**, 1713–1733, https://doi.org/10.1175/JCLI4082.1.

Lavers, D. A., and G. Villarini, 2013: Atmospheric rivers and flooding over the central United States. *J. Climate*, **26**, 7829–7836, https://doi.org/10.1175/JCLI-D-13-00212.1.

Lin, Y., and K. E. Mitchell, 2005: The NCEP stage II/IV hourly precipitation analyses: Development and applications. *19th Conf. on Hydrology*, San Diego, CA, Amer. Meteor. Soc., 1.2, https://ams.confex.com/ams/Annual2005/techprogram/paper_83847.htm.

Lora, J. M., C. A. Shields, and J. J. Rutz, 2020: Consensus and disagreement in atmospheric river detection: ARTMIP global catalogues. *Geophys. Res. Lett.*, **47**, e2020GL089302, https://doi.org/10.1029/2020GL089302.

Mahoney, K., and Coauthors, 2016: Understanding the role of atmospheric rivers in heavy precipitation in the southeast United States. *Mon. Wea. Rev.*, **144**, 1617–1632, https://doi.org/10.1175/MWR-D-15-0279.1.

Markowski, P., and Y. Richardson, 2011: *Mesoscale Meteorology in Midlatitudes*. Vol. 2, John Wiley and Sons, 432 pp.

Mesinger, F., and Coauthors, 2006: North American Regional Reanalysis. *Bull. Amer. Meteor. Soc.*, **87**, 343–360, https://doi.org/10.1175/BAMS-87-3-343.

Miller, A. J., 1990: Flood hydrology and geomorphic effectiveness in the central Appalachians. *Earth Surf. Processes Landforms*, **15**, 119–134, https://doi.org/10.1002/esp.3290150203.

Monteverdi, J. P., C. A. Doswell III, and G. S. Lipari, 2003: Shear parameter thresholds for forecasting tornadic thunderstorms in northern and central California. *Wea. Forecasting*, **18**, 357–370, https://doi.org/10.1175/1520-0434(2003)018<0357: SPTFFT>2.0.CO;2.

Moore, B. J., P. J. Neiman, F. M. Ralph, and F. E. Barthold, 2012: Physical processes associated with heavy flooding rainfall in Nashville, Tennessee, and vicinity during 1–2 May 2010: The role of an atmospheric river and mesoscale convective systems. *Mon. Wea. Rev.*, **140**, 358–378, https://doi.org/10.1175/ MWR-D-11-00126.1.

Musselman, K. N., F. Lehner, K. Ikeda, M. P. Clark, A. F. Prein, C. Liu, M. Barlage, and R. Rasmussen, 2018: Projected increases and shifts in rain-on-snow flood risk over western North America. *Nat. Climate Change*, **8**, 808–812, https://doi. org/10.1038/s41558-018-0236-4.

Nayak, M. A., and G. Villarini, 2017: A long-term perspective of the hydroclimatological impacts of atmospheric rivers over the central United States. *Water Resour. Res.*, **53**, 1144–1166, https://doi.org/10.1002/2016WR019033.

Nelson, B. R., O. P. Prat, D.-J. Seo, and E. Habib, 2016: Assessment and implications of NCEP Stage IV quantitative precipitation estimates for product intercomparisons. *Wea. Forecasting*, **31**, 371–394, https://doi.org/10.1175/WAF-D-14-00112.1.

Newell, R. E., N. E. Newell, and Y. Zhu, 1992: Tropospheric rivers? A pilot study. *Geophys. Res. Lett.*, **19**, 2401–2404, https://doi.org/10.1029/92GL02916.

Nielsen, E. R., and R. S. Schumacher, 2018: Dynamical insights into extreme short-term precipitation associated with supercells and mesovortices. *J. Atmos. Sci.*, **75**, 2983–3009, https:// doi.org/10.1175/JAS-D-17-0385.1.

——, and ——, 2020a: Dynamical mechanisms supporting extreme rainfall accumulations in the Houston "Tax Day" flood. *Mon. Wea. Rev.*, **148**, 83–109, https://doi.org/10.1175/MWR-D-19-0206.1.

——, and ——, 2020b: Observations of extreme short-term precipitation associated with supercells and mesovortices. *Mon. Wea. Rev.*, **148**, 159–182, https://doi.org/10.1175/MWR-D-19-0146.1.

Oakley, N. S., J. T. Lancaster, M. L. Kaplan, and F. M. Ralph, 2017: Synoptic conditions associated with cool season post-fire debris flows in the transverse ranges of Southern California. *Nat. Hazards*, **88**, 327–354, https://doi.org/10.1007/s11069-017-2867-6.

Payne, A. E., and Coauthors, 2020: Responses and impacts of atmospheric rivers to climate change. *Nat. Rev. Earth Environ.*, **1**, 143–157, https://doi.org/10.1038/s43017-020-0030-5.

Pohlert, T., 2018: Non-parametric trend tests and change-point detection. R package version 1.1.1, 18 pp., https://CRAN.R-project. org/package=trend.

Ralph, F. M., and Coauthors, 2019: A scale to characterize the strength and impact of atmospheric rivers. *Bull. Amer. Meteor. Soc.*, **100**, 269–289, https://doi.org/10.1175/BAMS-D-18-0023.1.

——, M. D. Dettinger, J. J. Rutz, and D. E. Waliser, 2020: *Atmospheric Rivers.* 1st ed. Springer, 252 pp.

Reimel, K. J., and M. Kumjian, 2021: Evaluation of K_{DP} estimation algorithm performance in rain using a known-truth framework. *J. Atmos. Oceanic Technol.*, **38**, 587–605, https:// doi.org/10.1175/JTECH-D-20-0060.1.

Romine, G. S., D. W. Burgess, and R. B. Wilhelmson, 2008: A dual-polarization-radar-based assessment of the 8 May 2003 Oklahoma City area tornadic supercell. *Mon. Wea. Rev.*, **136**, 2849–2870, https://doi.org/10.1175/2008MWR2330.1.

Rose, S. F., P. V. Hobbs, J. D. Locatelli, and M. T. Stoelinga, 2004: A 10-yr climatology relating the locations of reported tornadoes to the quadrants of upper-level jet streaks. *Wea. Forecasting*, **19**,

301–309, https://doi.org/10.1175/1520-0434(2004)019<0301: AYCRTL>2.0.CO;2.

Ryzhkov, A., P. Zhang, P. Bukovčić, J. Zhang, and S. Cocks, 2022: Polarimetric radar quantitative precipitation estimation. *Remote Sens.*, **14**, 1695, https://doi.org/10.3390/rs14071695.

Schumacher, R. S., and K. L. Rasmussen, 2020: The formation, character and changing nature of mesoscale convective systems. *Nat. Rev. Earth Environ.*, **1**, 300–314, https://doi.org/10. 1038/s43017-020-0057-7.

Shields, C. A., and Coauthors, 2018: Atmospheric River Tracking Method Intercomparison Project (ARTMIP): Project goals and experimental design. *Geosci. Model Dev.*, **11**, 2455–2474, https://doi.org/10.5194/gmd-11-2455-2018.

Slinskey, E. A., P. C. Loikith, D. E. Waliser, B. Guan, and A. Martin, 2020: A climatology of atmospheric rivers and associated precipitation for the seven U.S. national climate assessment regions. *J. Hydrometeor.*, **21**, 2439–2456, https://doi.org/ 10.1175/JHM-D-20-0039.1.

Slivinski, L. C., and Coauthors, 2019: Towards a more reliable historical reanalysis: Improvements for version 3 of the Twentieth Century Reanalysis system. *Quart. J. Roy. Meteor. Soc.*, **145**, 2876–2908, https://doi.org/10.1002/qj.3598.

Smith, J. A., E. Hui, M. Steiner, M. L. Baeck, W. F. Krajewski, and A. A. Ntelekos, 2009: Variability of rainfall rate and raindrop size distributions in heavy rain. *Water Resour. Res.*, **45**, W04430, https://doi.org/10.1029/2008WR006840.

——, M. L. Baeck, A. A. Ntelekos, G. Villarini, and M. Steiner, 2011a: Extreme rainfall and flooding from orographic thunderstorms in the central Appalachians. *Water Resour. Res.*, **47**, W04514, https://doi.org/10.1029/2010WR010190.

——, G. Villarini, and M. L. Baeck, 2011b: Mixture distributions and the climatology of extreme rainfall and flooding in the eastern US. *J. Hydrometeor.*, **12**, 294–309, https://doi.org/10. 1175/2010JHM1242.1.

——, M. L. Back, L. Yang, J. Signell, E. Morin, and D. C. Goodrich, 2019: The paroxysmal precipitation of the desert: Flash floods in the southwestern United States. *Water Resour. Res.*, **55**, 10 218–10 247, https://doi.org/10.1029/2019WR025480.

Smith, T. M., and Coauthors, 2016: Multi-radar multi-sensor (MRMS) severe weather and aviation products: Initial operating capabilities. *Bull. Amer. Meteor. Soc.*, **97**, 1617–1630, https://doi.org/10.1175/BAMS-D-14-00173.1.

Song, F., G. J. Zhang, V. Ramanathan, and L. R. Leung, 2022: Trends in surface equivalent potential temperature: A more comprehensive metric for global warming and weather extremes. *Proc. Natl. Acad. Sci. USA*, **119**, e2117832119, https:// doi.org/10.1073/pnas.2117832119.

Su, Y., and J. A. Smith, 2021: An atmospheric water balance perspective on extreme rainfall potential for the contiguous US. *Water Resour. Res.*, **57**, e2020WR028387, https://doi.org/10. 1029/2020WR028387.

——, ——, and G. Villarini, 2023: The hydrometeorology of extreme floods in the lower Mississippi River. *J. Hydrometeor.*, **24**, 203–219, https://doi.org/10.1175/JHM-D-22-0024.1.

Uccellini, L. W., and D. R. Johnson, 1979: The coupling of upper and lower tropospheric jet streaks and implications for the development of severe convective storms. *Mon. Wea. Rev.*, **107**, 682–703, https://doi.org/10.1175/1520-0493(1979)107<0682:TCOUAL> 2.0.CO;2.

Van Den Broeke, M. S., 2021: Polarimetric radar characteristics of tornadogenesis failure in supercell thunderstorms. *Atmosphere*, **12**, 581, https://doi.org/10.3390/atmos12050581.

——, 2015: Polarimetric tornadic debris signature variability and debris fallout signatures. *J. Appl. Meteor. Climatol.*, **54**, 2389–2405, https://doi.org/10.1175/JAMC-D-15-0077.1.

Wang, Y., and V. Chandrasekar, 2009: Algorithm for estimation of the specific differential phase. *J. Atmos. Oceanic Technol.*, **26**, 2565–2578, https://doi.org/10.1175/2009JTECHA1358.1.

Westra, S., and Coauthors, 2014: Future changes to the intensity and frequency of short-duration extreme rainfall. *Rev. Geophys.*, **52**, 522–555, https://doi.org/10.1002/2014RG000464.

Wilson, M. B., and M. S. Van Den Broeke, 2021: An automated Python algorithm to quantify Z_{DR} arc and K_{DP}-Z_{DR} separation signatures in supercells. *J. Atmos. Oceanic Technol.*, **38**, 371–386, https://doi.org/10.1175/JTECH-D-20-0056.1.

——, N. R. Humrich, and M. S. Van Den Broeke, 2020: The Supercell Polarimetric Observation Research Kit (SPORK): An automated, python-based algorithm for examining supercell dual-pol signatures. *10th Symp. on Advances in Modeling and Analysis Using Python*, Boston, MA, Amer. Meteor. Soc., 2.5, https://ams.confex.com/ams/2020Annual/webprogram/Paper367028.html.

Zhu, Y., and R. E. Newell, 1998: A proposed algorithm for moisture fluxes from atmospheric rivers. *Mon. Wea. Rev.*, **126**, 725–735, https://doi.org/10.1175/1520-0493(1998)126<0725:APAFMF>2.0.CO;2.

Zipser, E. J., and C. Liu, 2021: Extreme convection vs. extreme rainfall: A global view. *Curr. Climate Change Rep.*, **7**, 121–130, https://doi.org/10.1007/s40641-021-00176-0.